Magnetic-field-directed Self-assembly of Multifunctional Aerosol Nanoparticles

Preger, Calle

2020

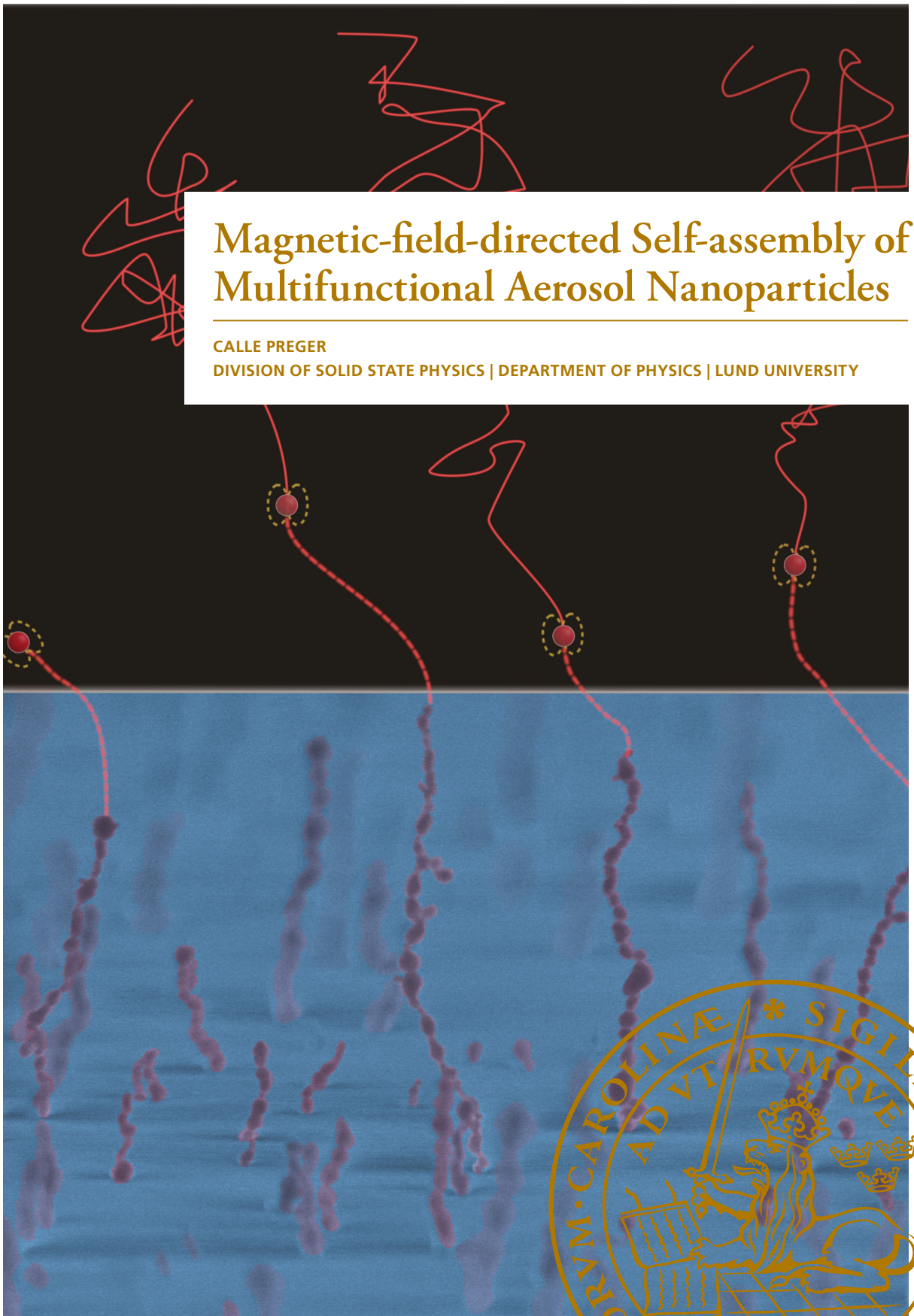

Magnetic-field-directed Self-assembly of Multifunctional Aerosol Nanoparticles

CALLE PREGER
DIVISION OF SOLID STATE PHYSICS | DEPARTMENT OF PHYSICS | LUND UNIVERSITY

Printed by Media-Tryck, Lund 2020 NORDIC SWAN ECOLABEL 3041 0903

Lund University
Faculty of Engineering
Department of Physics

ISBN 978-91-7895-668-5

Magnetic-field-directed Self-assembly of Multifunctional Aerosol Nanoparticles

Calle Preger

LUND
UNIVERSITY

DOCTORAL DISSERTATION

Which by due permission of the Faculty of Engineering, Lund University, Sweden, will be publicly defended Friday 27th of November, 2020, at 9:15 in the Rydberg Lecture hall at the Department of Physics, Sölvegatan 14, Lund, Sweden.

Faculty opponent
Associate Professor Adam Boies
University of Cambridge

Organization	Document name
LUND UNIVERSITY	DOCTORAL DISSERTATION
Department of Physics PO Box 118 SE-22100 LUND SWEDEN	Date of disputation 2020-11-27
Author(s) Calle Preger	Sponsoring organization

Title

Magnetic-field-directed Self-assembly of Multifunctional Aerosol Nanoparticles

Abstract

The work described in this dissertation covers the entire process from the generation of single- and multicomponent aerosol nanoparticles, via deposition and self-assembly, to potential applications. Engineered aerosol nanoparticles are promising for many technological applications, including catalysis, surface coatings, sensors, and semiconducting structures. Aerosol generation allows the size-selection of nanoparticles, and their shape and composition can be changed and studied in the gas flow. Another advantage of aerosol nanoparticle generation is that it enables simple transfer from the gas phase to the desired substrate in a continuous way. Aerosol generation is thus a useful way of synthesizing tailored nanoparticles, and assembling them into nanostructures in a highly controlled way.

In this work, single- and multicomponent magnetic nanoparticles were generated, and their structure and composition studied in detail. The aerosol nanoparticles were generated by spark ablation, a fast and continuous method of producing aerosol nanoparticles with great capability of combining and mixing different materials to form nanoparticles. The influence of the carrier gas on the final structure of the nanoparticles was studied, and it was shown how evaporation of a component in the nanoparticles could change their composition.

The deposition and self-assembly of magnetic aerosol nanoparticles were also studied. It was shown how the direction of an external magnetic field could be used to direct the self-assembly of magnetic aerosol nanoparticles during deposition. Differently oriented nanostructures could be assembled by changing the magnetic field direction, and integrated directly onto a substrate. In order to study and quantify this self-assembly, it was necessary to estimate the concentration of nanoparticles on the substrate. This depends on the nanoparticle concentration in the gas, which can easily be monitored, and the size of the deposition spot, which depends on several parameters. The exact relation between the spot size and the deposition parameters was found by performing COMSOL Multiphysics simulations and comparing the results to those obtained with experimental depositions. With this developed formula it is possible to predict the deposited nanoparticle concentration on the substrate without the need for off-line analysis.

Finally, the possibility of forming multifunctional nanostructures by the self-assembly of multicomponent aerosol nanoparticles was explored. As a proof of concept, the catalytic activity of self-assembled CoPd nanoparticles was measured and compared to that of Pd nanoparticles. In future studies, the composition and size of multifunctional nanoparticles, together with the alignment of the multifunctional nanochains, can be fine-tuned in order to form nanostructures for specific applications.

Key words

nanoparticles, aerosol, magnetic nanoparticles, directed self-assembly, electrostatic precipitation, spark ablation

Classification system and/or index terms (if any)

Supplementary bibliographical information		Language English
ISSN and key title		ISBN 978-91-7895-668-5 (print) 978-91-7895-669-2 (pdf)
Recipient's notes	Number of pages 148	Price
	Security classification	

Signature  Date 2020-10-19

Magnetic-field-directed Self-assembly of Multifunctional Aerosol Nanoparticles

Calle Preger

LUND
UNIVERSITY

Cover photo by Calle Preger

Division of Solid State Physics, Department of Physics

ISBN: 978-91-7895-668-5 (print)
ISBN: 978-91-7895-669-2 (pdf)

Printed in Sweden by Media-Tryck, Lund University
Lund 2020

Abstract

The work described in this dissertation covers the entire process from the generation of single- and multicomponent aerosol nanoparticles, via deposition and self-assembly, to potential applications. Engineered aerosol nanoparticles are promising for many technological applications, including catalysis, surface coatings, sensors, and semiconducting structures. Aerosol generation allows the size-selection of nanoparticles, and their shape and composition can be changed and studied in the gas flow. Another advantage of aerosol nanoparticle generation is that it enables simple transfer from the gas phase to the desired substrate in a continuous way. Aerosol generation is thus a useful way of synthesizing tailored nanoparticles, and assembling them into nanostructures in a highly controlled way.

In this work, single- and multicomponent magnetic nanoparticles were generated, and their structure and composition studied in detail. The aerosol nanoparticles were generated by spark ablation, a fast and continuous method of producing aerosol nanoparticles with great capability of combining and mixing different materials to form nanoparticles. The influence of the carrier gas on the final structure of the nanoparticles was studied, and it was shown how evaporation of a component in the nanoparticles could change their composition.

The deposition and self-assembly of magnetic aerosol nanoparticles were also studied. It was shown how the direction of an external magnetic field could be used to direct the self-assembly of magnetic aerosol nanoparticles during deposition. Differently oriented nanostructures could be assembled by changing the magnetic field direction, and integrated directly onto a substrate. In order to study and quantify this self-assembly, it was necessary to estimate the concentration of nanoparticles on the substrate. This depends on the nanoparticle concentration in the gas, which can easily be monitored, and the size of the deposition spot, which depends on several parameters. The exact relation between the spot size and the deposition parameters was found by performing COMSOL Multiphysics simulations and comparing the results to those obtained with experimental depositions. With this developed formula it is possible to predict the deposited nanoparticle concentration on the substrate without the need for off-line analysis.

Finally, the possibility of forming multifunctional nanostructures by the self-assembly of multicomponent aerosol nanoparticles was explored. As a proof of concept, the catalytic activity of self-assembled CoPd nanoparticles was measured and compared to that of Pd nanoparticles. In future studies, the composition and size of multifunctional nanoparticles, together with the alignment of the multifunctional nanochains, can be fine-tuned in order to form nanostructures for specific applications.

Populärvetenskaplig sammanfattning

Den här avhandlingen handlar om att skapa specialdesignade luftburna magnetiska nanopartiklar och att genom kontrollerad infångning, ansamla dem till större nanostrukturer bestående av långa nanokedjor. De magnetiska egenskaperna hos nanopartiklarna gör att de kraftigt attraheras till varandra och linjerar upp sig till nanokedjor. Figur 1a visar hur enstaka kedjor bestående av nanopartiklar reser sig från ytan för att sedan spänna upp stora nätverk bestående av långa kedjor (Figur 1b-c). Genom att variera innehållet i de magnetiska nanopartiklarna kan deras egenskaper förändras och specialutformade nanokedjor med unika funktioner för olika användningsområden bildas.

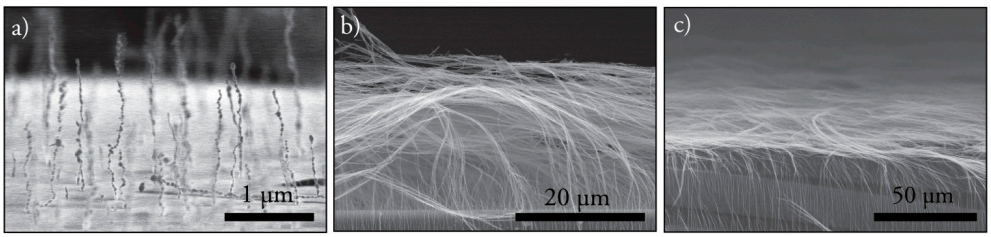

Figur 1. Luftburna magnetiska nanopartiklar ansamlas till stående nanokedjor på grund av den starka magnetiska attraktionen (a). De allt fler infångade nanopartiklarna ansamlas efterhand till stora nätverk bestående av långa nanokedjor med potentiell användning för katalytiska reaktioner (b-c).

Strukturbildningarna i Figur 1 är intressanta eftersom nanopartiklarnas egenskaper kan komma att utnyttjas mer effektivt när de ansamlas på detta vis. Exempelvis kan denna typ av struktur användas för att få nanopartiklarna att enklare komma i kontakt med gasmolekylerna i luften. Oftast har gasmolekylerna i luften svårt att ta sig ner till platta ytor där flödeshastigheten är låg, men genom att låta nanopartiklarna sträcka sig högt ovan ytan, kan fler nanopartiklar på ett mer effektivt vis komma i kontakt med gasmolekylerna i luften. Denna kontakt mellan gasmolekylerna och nanopartiklarna är oerhört viktig för att möjliggöra nanopartiklarnas speciella funktion som t.ex. kan vara som katalysator vid kemiska reaktioner.

Vad är då en katalysator? katalysatorer är något som underlättar en kemisk reaktion utan att tillföra någon extra energi till systemet, och dessa är viktiga för många processer. En katalysator kan t.ex. vara kemiska molekyler eller en ansamling av partiklar. Förbättring och effektivisering av nuvarande katalysatorer leder till att man kan utföra samma kemiska reaktioner fast med lägre energikostnad, och på så vis bespara både resurser och miljö. De katalytiska reaktionerna sker på katalysatorns yta eftersom deras yta är i direkt kontakt med molekylerna som ska påverkas. Partiklar och framförallt nanopartiklar har visat sig vara mycket effektiva som katalysatorer, framförallt eftersom nanopartiklarnas yta är väldigt stor i jämförelse med deras volym.

Generellt sett gäller att desto mindre något är, desto större kommer deras yta att vara jämfört med deras volym. Denna effekt kan illustreras med ett äpple. Till en början utgör äpplets skal hela dess yta. Delar man äpplet mitt itu kommer äpplets innersida att exponeras, och den totala ytan öka samtidigt som volymen är densamma. För varje gång äpplet delas, kommer mer och mer yta exponeras och tillslut (förutsatt att man har en väldigt vass kniv) når man till storleken hos en nanopartikel. En nanopartikel kan ha en diameter mellan 1 och 100 nanometer (nm), där en (1) nm motsvarar en miljardels (10^{-9}) meter. För att sätta det i ett perspektiv så motsvarar en (1) nm ungefär fyra uppradade järnatomer, medan 100 nm är den ungefärliga storleken på det eländiga Coronaviruset. För att skapa och studera så små partiklar krävs det avancerade framställnings- och analysmetoder, och detta har utvecklats enormt mycket de senaste 50 åren. Denna avhandling bidrar till denna utveckling genom att fortsätta att utforska framställning av specialdesignade nanopartiklar, samt genom att presentera en ny metod för att ansamla nanopartiklar till skräddarsydda nanostrukturer genom att kombinera elektriska och magnetiska fält.

Nanopartiklarna som har studerats för denna avhandling är till en början luftburna (så kallade aerosoler). En viktig del i framställandet är därför att kunna fånga in nanopartiklarna på ett kontrollerat och effektivt vis. Infångningen av de luftburna elektriskt laddade nanopartiklarna har utförts med hjälp av ett starkt elektriskt fält som drar ner nanopartiklarna mot en yta. Med denna metod kommer alla luftburna nanopartiklarna att hamna inom en cirkulär fläck på ytan. För att effektivisera denna infångning har jag genom experiment och simuleringar tagit fram en ny ekvation som kan förutspå infångningsfläckens storlek. Med hjälp av denna ekvation kan man minimera slöseri med nanopartiklar och optimera infångningstiden.

För ytterligare kontroll av infångningen har jag kombinerat det elektriska fältet med ett magnetiskt fält. Det elektriska fältet är aktivt vid infångningen av nanopartiklarna från gasen, medan det magnetiska fältet kommer finjustera placeringen av de enskilda magnetiska nanopartiklarna när de närmar sig ytan. De magnetiska nanopartiklarna kommer att attrahera varandra med samma typ av kraft som två rödvita stavmagneter. En magnetisk nanopartikel som redan har placerats på ytan kommer därför kraftigt attrahera de inkommande nanopartiklarna och dra dem till sig. På så vis kommer kedjor av nanopartiklar (nanokedjor) bildas, och riktningen på det magnetiska fältet kommer att avgöra vilken riktning som de magnetiska nanokedjorna breder ut sig i.

För att nanostrukturerna och nanokedjorna ska få specialdesignade egenskaper, är det viktigt att bemästra framställningen av nanopartiklarna. Genom att styra framställningen och noga analysera de framtagna magnetiska nanopartiklarna kan specialdesignade nanopartiklar som innehåller flera olika sorters ämnen skapas. Dessa nanopartiklar kan få unika egenskaper, och de ansamlade nanostrukturerna kan på så vis bli multifunktionella.

T.ex. kan de magnetiska nanopartiklarna blandas med en delmängd katalytiskt ämne, för att göra nanostrukturerna katalytiskt aktiva mot en speciell miljö.

Denna avhandling handlar om processen från skapandet av nanopartiklarna, till infångandet och ansamlingen av nanostrukturerna och dessa olika steg illustreras i Figur 2. Denna avhandling bidrar med ny kunskap om framställningen av luftburna nanopartiklar, samt hur dessa kan ansamlas på ett kontrollerat vis. Detta utgör en grund för fortsatta studier om ansamling av luftburna magnetiska nanopartiklar med skräddarsydda egenskaper.

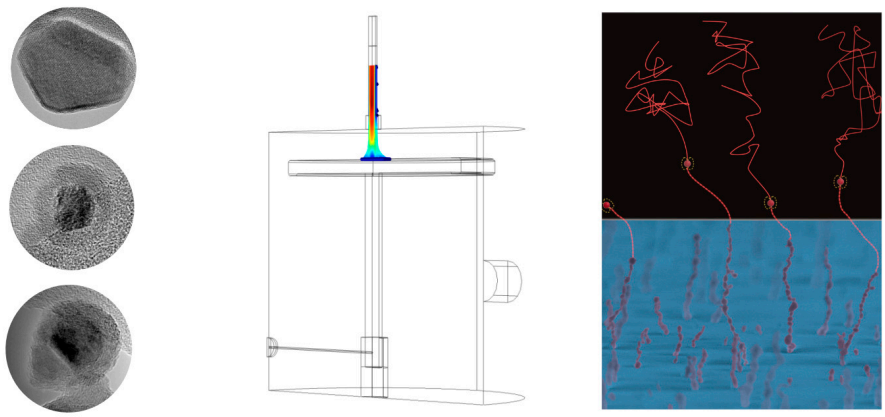

Figur 2. De olika delarna i framställandet av multifunktionella nanostrukturer. Först skapas nanopartiklar som kan innehålla flera olika ämnen. Därefter sker en kontrollerad infångning av de luftburna nanopartiklarna genom att utsätta dem för ett stark elektriskt fält som drar nanopartiklarna mot en yta. Slutligen ansamlas nanopartiklarna på ytan där de starka krafterna mellan de magnetiska nanopartiklarna drar dem mot varandra för att forma nanokedjor som breder ut sig i samma riktning som det magnetiska fältet.

List of papers

This dissertation is based on the following papers. The papers are referred to in the text by their Roman numerals

Paper I. **Controlled oxidation and self-passivation of bimetallic magnetic FeCr and FeMn aerosol nanoparticles**
C. Preger, C Bulbucan, B. O. Meuller, L. Ludvigsson, A. Kostanyan, M. Muntwiler, K. Deppert, R. Westerström, M. E. Messing
The Journal of Physical Chemistry C, **2019**, 123, 26, 16083-16090

I conceived the project together with my three supervisors M.E.M, R.W and K.D. I performed all the experimental work and data analysis, apart from the magnetic measurements. I wrote the entire paper with help from my co-authors.

Paper II. **Predicting the deposition spot radius and the nanoparticle concentration distribution in an electrostatic precipitator**
C. Preger, N. C. Overgaard, M. E. Messing, M. H. Magnusson
Aerosol Science and Technology, **2020,** 54, 6**,** 718-728

I initiated the project together with M.H.M. I designed the experiments and performed all the experimental work, including the COMSOL Multiphysics simulations. N.C.O performed the analytical analysis, and is the main contributor to that part of the paper. I wrote the other parts, and was responsible for the entire paper with help from my co-authors.

Paper III. **Bottom-up field-directed self-assembly of magnetic nanoparticles into ordered nano- and macrostructures**
C. Preger, M. Josefsson, R. Westerström, M. E. Messing
Submitted manuscript

I conceived the study, designed and initiated the project, and performed all the experimental work. The code for the simulations was developed by M.J, but I took an active part in designing the numerical model. I wrote the entire paper with help from my co-authors

Abbreviations

DMA – differential mobility analyzer

ESP – electrostatic precipitator

MESP – magnetic-field-assisted electrostatic precipitator

PLIF – planar laser-induced fluorescence

SEM – scanning electron microscopy

STEM – scanning transmission electron microscopy

TEM – transmission electron microscopy

XEDS – x-ray energy dispersive spectroscopy

XPS – x-ray photoemission spectroscopy

Acknowledgements

This dissertation would not have been possible without all the help and support from the people around me. I feel very privileged to have worked in an environment where so many are helpful and kind. The list of names would be very long if I should mention everyone that helped me during these last five years. To all of you, I am very grateful. Of course, some people have contributed and supported me substantially.

First and foremost, my warmest thanks to **Maria** for being a remarkably great supervisor and mentor. Your kindness and endless support have made my life as a PhD-student feel trouble-free and easy. You always encouraged my different side-projects, and gave me plenty of freedom to develop as a researcher. You were also always present when I needed you the most. Working close with you over the last five years have been a fun and inspiring journey.

I would also like to thank my co-supervisors. To **Rasmus,** for all the interesting discussions in your office that never turned out as planned. Your ability to listen and discuss science have encouraged and inspired me to brainstorm new research ideas with you. To **Knut**, who introduced me to the world of aerosols, but also demonstrated how to master mingle events at conferences. You have helped me obtain a broader network, and made my research visit at Seoul National University possible. Mentioning Seoul, I am very grateful that **Prof. Mansoo Choi** took me in for a research visit in his group, and I would like to express my gratitude to **Wooik** for taking great care of me during these months. I wish you the best in life and research.

To **Martin M,** who encouraged and helped me with all my COMSOL struggles, and to **Niels Christian,** who took our suggested and incomplete "exam problem", and turned it into a beautiful mathematical solution. Our collaboration really demonstrates the beauty of openness and helpfulness.

I would also like to thank all the former and current members in our constantly growing aerosol group at FTF. The way we always support each other in various ways is something I have always appreciated. To **Bengt**, for building and taking care of our outstanding aerosol generator, and always providing solutions when I failed to make it work. To **Linus** and **Robert,** who were accommodating and patient when I first started out as a PhD-student and everything was new to me. To **Sara F**, **Sudha**, **Markus**, **Namsoon,** and **Sara B,** for being the nicest friends and colleagues. To **Pau** and **Marie**, who I recently got to know, and I am certain will be a great contribution to the aerosol group.

A warm thanks to all the helpful and kind people at FTF. You all contribute to create a caring and inspiring working environment. To all my colleagues at EAT, that always made me feel included, and for being great company at all the aerosol conferences.

Without you, these conferences would not have been a yearly highlight, and I would not have had equally as many great memories.

A special thanks to **Martin J**, not only for being a wonderful friend, but also for being a great colleague and collaborator. Your knowledge is impressive, and you have helped me with innumerous physics related problems during the years. I can honestly state that discussing research over a few beers has proven to be a proper way of conducting research.

During my 10 years at Lund University, I have made many long lasting friendships. I feel grateful having so many wonderful friends in my life and I would like to thank you all. This also includes my wonderful choir, including all former and current members. I also want to acknowledge the Dr. Nano crew for all our Friday lunches where we shared our insights and struggles.

I wish to thank my family for always supporting and believing in me, and telling me that anything is possible. Finally, to **Elina,** my dearest friend and life partner, together with you, life could not be better.

Contents

1. Introduction

One of the most impressive skills of humankind is the ability to design and construct extraordinary structures. Examples of this are the pyramids and cities that were designed and constructed thousands of years ago. On a much smaller scale, chemists have long been able to assemble small molecules into larger structures with specific properties. Nanoscience is on a scale somewhat larger than most smaller molecules, an is still considered a young research field, however, considerable developments have been achieved during the past 50 years making it possible to synthesize novel nanostructures with great precision.

But why are we interested in nanoscience? Materials on this scale can exhibit properties that differ from those of the bulk material. The optical, magnetic, and electrical properties of some kinds of nanoparticles depend on their size, and a desired property can thus be obtained by fine-tuning the nanoparticles during the synthesis. Another reason why nanoparticles and nanostructures are interesting is their high surface-to-volume ratio, making them effective reactants, and of great use, for example, in catalytic reactions. Finally, another reason for studying nanostructures is that smaller structures require less space. Controlled nanoparticle generation could for example, be utilized in 3D printing of nanostructures for future integrated circuits.

In this dissertation, I describe the generation and assembly of engineered aerosol nanoparticles. Aerosol nanoparticles are used as tiny building blocks to construct specialized nanostructures with potential for use in catalytic reactions. The assembly of the magnetic nanoparticles is controlled by magnetic-field-directed self-assembly in an electric field. In order to do this, the nanoparticles must be aerosolized (i.e. suspended in a gas), charged, and have a strong magnetization prior to self-assembly. By fine-tuning nanoparticle generation, a magnetic material can be mixed with other elements to form multicomponent nanoparticles that retain the ability to self-assemble into larger nanostructures. At the same time, these nanostructures will have a new unique feature based on the properties of the other introduced component, and multifunctional nanostructures with specialized properties can thus be constructed.

To successfully construct multifunctional nanostructures, it is important to understand and be able to control all stages of the synthesis. Firstly, and perhaps most importantly, the generation of multicomponent aerosol nanoparticles must be understood, since these

are the building blocks used to make larger nanostructures. Secondly, it must be possible to capture the nanoparticles from the gas efficiently and place them on a substrate. Finally, to obtain the unique and desired properties of the nanostructures, it is important to be able to design and control the way in which the nanoparticles assemble on the substrate to form the nanostructures. All these stages are described thoroughly in this dissertation, starting with the generation of engineered aerosol nanoparticles.

Engineered aerosol nanoparticles – Forming the building blocks

Engineered nanoparticle generation is a broad field, and can be approached in various ways using mechanical, liquid-based, vacuum, or gas-phase methods. Gas-phase synthesis of nanoparticles, also referred to as aerosol synthesis, is a quick and versatile method allowing the simple and continuous transfer of nanoparticles from the gas phase to the desired substrate. An aerosol is a two-phase system consisting of particles suspended in a gas, with particle sizes ranging from a few nm to 100 μm[1]. The particles must be stable in the gas for at least a few seconds for it to be considered an aerosol. Aerosol physics is highly relevant in many of the most important problems the world is facing today, including climate change, air pollution, and virus transmission, as well as technological applications[2].

Engineered aerosol nanoparticles can be generated for technological applications in many different ways. Among the most frequently used synthesis methods are flame spray synthesis, evaporation, laser ablation, and spark ablation[3,4]. Aerosol nanoparticles engineered in this way can be used in many different applications, including coating of surfaces[5], the production of antibacterial textiles[6,7], and as fertilizers in agriculture[8]. Aerosol generated nanoparticles can also be used to construct specialized semiconducting nanostructures[9,10], or as catalysts for scaled-up carbon nanotube generation[11]. A benefit of aerosol generation is the possibility of influencing the aerosol nanoparticles in-flight, and changing many of their properties as they are carried by the gas flow. The surface of the particles can, for instance, be modified in-flight by applying a metal[12] or polymer coating[13].

Multicomponent nanoparticles – Combining material properties

Engineered nanoparticles often consist of a single component. However, research is increasingly being performed on generating multicomponent nanoparticles, and it is likely that alloy or hybrid nanoparticles will have the most interesting properties. Although combining several elements in nanoparticles increasing the complexity of

controlling their generation, it also paves the way for new materials and systems with unique properties.

Aerosol generation, by spark ablation in particular, which is the method used for nanoparticle generation throughout this work, has proven to be a useful method of combining several different elements into a single particle. Immiscible elements can be mixed[14] and nanoparticles composed of more than six different elements can be synthesized[15–17]. The different components can also be mixed in many different ways. When the components are mixed on an atomic level, and occupy the same lattice structure, the nanoparticles are considered as true alloys. These specialized alloys can be used to enhance, combine, or fine-tune material properties. For instance, the magnetic and optical properties of Heusler systems, where three different components are mixed to form an alloy, depend on the total number of valence electrons in the system[18–21]. It is also possible to combine materials in the same nanoparticle so that they have the combined properties of the different materials. Such nanoparticles are referred to as multifunctional nanoparticles.

Multifunctional nanoparticles – The best of two worlds

Multifunctional nanoparticles are of interest due to their combined properties within the same structure. In multifunctional nanoparticles it is possible to tailor the desired properties through the choice of the material used. Multifunctional nanoparticles can be synthesized into different shapes. Common types are core-shell and Janus, as illustrated in Figure 1.1. In core-shell nanoparticles, one component occupies the core of the particle and the other component makes up the surface[22]. Core-shell nanoparticles have many functions, for example, when the inner core needs protection[13], or when an expensive reactant is only needed on the surface[23]. It can be used when the combined properties of the two elements are required, for example, a magnetic core combined with a catalytic shell[24–26], or when the interaction between the core and shell results in new combined properties[27–30].

The Janus-type structure having a separation of the components into different sides within the same nanoparticle[31]. In contrast to the core-shell nanoparticles, both components in the Janus structure occupy the surface. Janus nanoparticles are synthesized when the combined properties of the two components are desired[32], or when the interaction between the two components changes the properties of the nanoparticles[33].

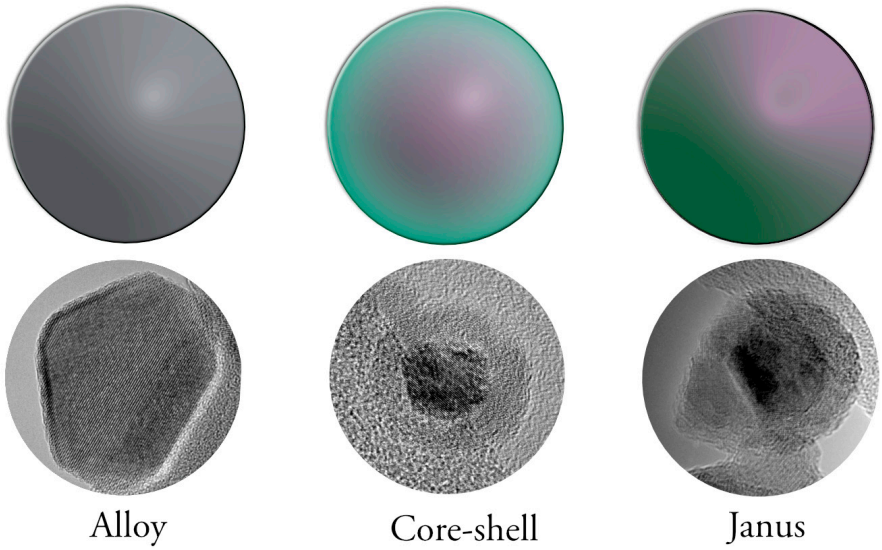

Figure 1.1. Combining materials in a nanoparticle can result in different types of structures. If the different materials are mixed on an atomic level and occupy the same lattice structure, the nanoparticles are considered a true alloy. It is also common for the different materials to separate into different regions. In core-shell nanoparticles one material occupies the inner core while the other occupies the surface. In Janus nanoparticles the different materials are separated on two different sides of the nanoparticles.

Assembly of aerosol nanoparticles – Construction

The collection of particles is an essential part of aerosol science and technology. This can be performed in various ways, depending on the size, structure, and properties of the aerosol. Larger micro- and macroparticles have high inertia, and settle due to the force of gravity. In a gas flow, such particles initially follow the trajectory of the gas, but if the direction of the flow changes suddenly, the larger particles will continue to follow the initial trajectory, and become deposited by impaction. This is achieved with an aerosol instrument called an impactor, where the particles are collected on a collection plate placed perpendicular to the gas flow[1]. Jet-printed structures with specific shape can be generated using a high gas velocity and a moveable nozzle[34].

Smaller particles, including nanoparticles, have low inertia, and are more difficult to capture by impaction. These particles follow the gas flow, regardless of changes in its flow direction. Additional forces are therefore necessary to capture and assemble such particles. This can be done using diffusional, thermophoretic or electrophoretic forces. Charged particles are effectively captured using electric fields. The advantage of using an electric field is that the applied field only affects the particles, and not the gas flow dynamics. This

technique is referred to as electrostatic precipitation, and the instrument is called an electrostatic precipitator (ESP) where a homogenous electric field is utilized to collect the incoming aerosol in a small spot. Advanced particle deposition and fine nanostructure formation, such as micropatterning[35,36] and 3D printing[37,38] can be performed by manipulating the electric field.

Controlled deposition – Avoiding wasting building blocks

The development of the ESP has enabled high efficiency in particle collection[39]. The charged nanoparticles enter with the gas and travel toward a collection plate. A high electric potential is applied to the plate, which creates an electric field that forces the nanoparticles towards the collection plate. The nanoparticles are collected in a circular spot on the plate (Figure 1.2). The deposited particle concentration on the plate depends on the size of this circular spot, which in turn depends on the deposition conditions. Unnecessary waste of particles can be avoided by predicting the size of this deposition spot, and the concentration and mass of the deposited nanoparticles can be estimated without the need for off-line analysis. Despite being a frequently used aerosol instrument for particle sampling, no researcher has previously been able to formulate the exact relation between the deposition parameters and the size of the deposition spot in an ESP.

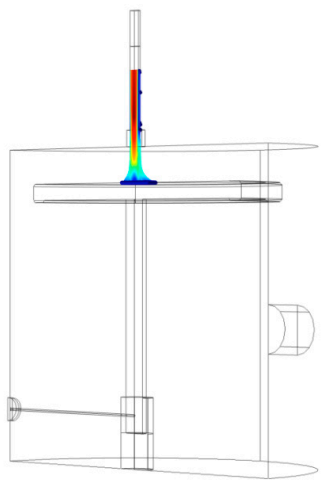

Figure 1.2. Cross-section of an ESP from COMSOL Multiphysics simulation when nanoparticle deposition was studied. The colored profile indicates the trajectory and velocity of the nanoparticles as they travel toward the collection plate. By predicting the deposition spot size in an ESP, the concentration and mass of the deposited nanoparticles can be estimated without the need for off-line analysis.

Directed self-assembly of nanostructures – Architecture

The homogeneous electric field in the ESP forces the nanoparticles towards the substrate where the gas velocity is low. Close to the substrate, the trajectories of the nanoparticles depend on the local environment. Local electric fields arising from surface treatment[35] or irregularities in the surface structure affect the nanoparticle distribution[40]. The already deposited nanoparticles may also influence the nanoparticles in the gas, as they can attract or repel nanoparticles in the gas depending on their charge or magnetic properties[41], as illustrated in Figure 1.3.

Magnetic nanoparticles experience a strong long-range dipole – dipole attraction, usually resulting in the formation of a chain structure. In 1963, in one early microscopy study on fine metal (nano)particles, Kimoto et al. noted that Fe, Ni, and Co particles arranged differently from other metals[42]. They suggested that these *remarkable 'necklace-like' arrangements* could be due to the ferromagnetic nature of the particles, and noted that the particles aligned in the presence of a magnetic field. This was later confirmed by the *in situ* observation of the formation of nanoparticles in chains (nanochains) in a magnetic field[43].

The strong dipole – dipole interactions between magnetic nanoparticles have been utilized to form advanced nanoparticle structures in the shape of single nanochains[44,45], bundles[46–49], and compact superstructures[50–52]. Such self-assembly of nanoparticles can be a powerful tool to achieve a strong collective behavior, while still retaining the properties of the individual nanoparticles[53]. Large ensembles of self-assembled nanostructures also have potential use for electrochemical energy storage[54] and catalytic reactions[46,55].

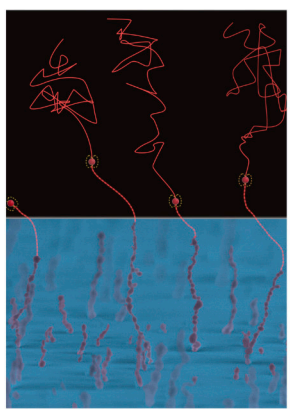

Figure 1.3. Illustration of the self-assembly and trajectory (red lines) of the nanoparticles in the gas. A scanning electron microscopy (SEM) image have been colored and modified to an illustration. The magnetic nanoparticles in the gas (red spheres) are attracted by the already deposited nanoparticles (red-colored SEM image). With an out-of-plane external magnetic field, the nanoparticles assemble into free-standing nanochains.

This dissertation describes the generation, deposition and self-assembly of engineered aerosol nanoparticles. Multicomponent nanoparticles were formed by spark ablation, enabling the combination of different materials into nanoparticles. The relation between the size of the deposition spot and the deposition variables was described by performing COMSOL Multiphysics simulations. Lastly, the self-assembly of magnetic multifunctional nanoparticles was performed in a combined electric and magnetic field. The magnetic field directs the self-assembly of the nanoparticles, and differently aligned nanostructures were formed depending on the direction of the magnetic field.

Outline

The outline of this dissertation follows the same route as the generation of the aerosol nanoparticles. **Chapter 2 – Spark ablation and nanoparticle generation** describes how the individual aerosol nanoparticles are formed; starting with the formation of the spark, followed by an illustration of how single- and multicomponent nanoparticles can be generated by spark ablation. The next two chapters, **Chapter 3 – The collection of aerosol nanoparticles** and **Chapter 4 – Self-assembly of magnetic aerosol nanoparticles**, describe the deposition and self-assembly of aerosol nanoparticles in a regular ESP and a magnetic-field-assisted ESP (MESP). The deposition in an ESP is described in **Chapter 3**, and a formula that predicts the spot size and the deposited particle concentration on the substrate is presented. **Chapter 4** describes how the self-assembly of magnetic nanoparticles can be achieved, and how the applied magnetic field is used to assemble the magnetic nanoparticles into highly controlled nanostructures. In **Chapter 5 – Multifunctional nanostructures**, the information in **Chapters 2-4** is combined to describe how multifunctional nanoparticles are formed and self-assembled into nanostructures. Finally, the conclusions and future outlook are presented in **Chapter 6.** The **Appendix** provides short technical descriptions of some of the measurement techniques used.

2. Spark ablation and nanoparticle generation

The advantages of engineered nanoparticle generation in the aerosol phase are that it is continuous, and that it is possible to modify the nanoparticles as they travel in the gas flow. The aerosol nanoparticle generation system used in this work is shown schematically in Figure 2.1. Many other instruments can also be added to the system. The instruments in this figure are used for the nanoparticle generation, compaction of agglomerates, size-selection, detection, and deposition. The instruments and steps involved are described in detail below.

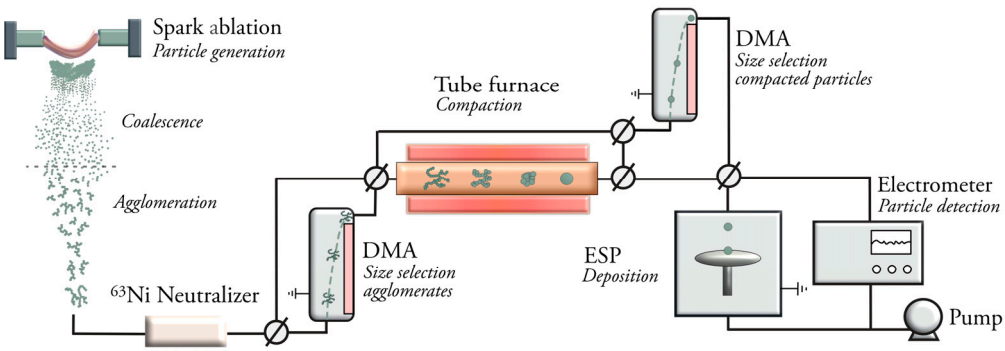

Figure 2.1. Schematic of aerosol nanoparticle generation. The nanoparticles are generated by spark ablation, and initially shaped as agglomerates. The agglomerates pass through a neutralizer where they attain a known charge distribution. Next, the agglomerates are compacted into a more spherical shape in the tube furnace. Before and after the tube furnace two differential mobility analyzers (DMAs) are used to size-select either the agglomerates or the compacted nanoparticles. Finally, the nanoparticle concentration is either measured with an electrometer, or the nanoparticles are deposited with an electrostatic precipitator (ESP).

The spark

Aerosol generation by spark ablation is a relatively new technique, and was described in detail for the first time in 1988 by Schwyn et al.[56]. The method is frequently referred to as being a *clean and green* method of generating nanoparticles[57–59], mainly because it requires

no chemicals and the gas can be recycled in the system. Details on nanoparticle generation by spark ablation, and many processing steps related to it, can be found in *Spark Ablation: Building Blocks for Nanotechnology* by A. Schmidt-Ott[60].

From spark to particle

The simplest, and perhaps most common, setup used for spark ablation is the rod-to-rod configuration. This is the configuration first described, and it was also the one used in this work. In the rod-to-rod configuration, two conducting rods, also referred to as electrodes, face each other, separated by a small gap, usually a few mm. The electrodes are connected to a simple electrical circuit, where one of the electrodes is charged, and the other is grounded. A high-voltage source delivers a constant current to the charged electrode, and to a capacitor placed in parallel with the electrodes. Charging is continuous, and provides the energy for the spark. The voltage difference between the two electrodes increases until it exceeds the breakdown voltage of the gas, governed by Paschen's Law. A current flow rapidly across the gap, the spark is generated, and strikes the opposing grounded electrode. The capacitor discharges, and the process is repeated[56,61,62].

Prior to each discharge, the gas molecules in the gap are ionized, and a plasma channel that carries the short current is formed between the electrodes. During the life-time of the spark, negative electrons and ions travel in one direction, and the heavier positive ions travel in the opposite direction[61]. When these high-energy ions strike the electrodes, the surface of the electrodes become locally heated to high temperatures, and material is ablated, creating small craters. Both microscopic and macroscopic craters are formed[63,64], as shown in Figure 2.2.

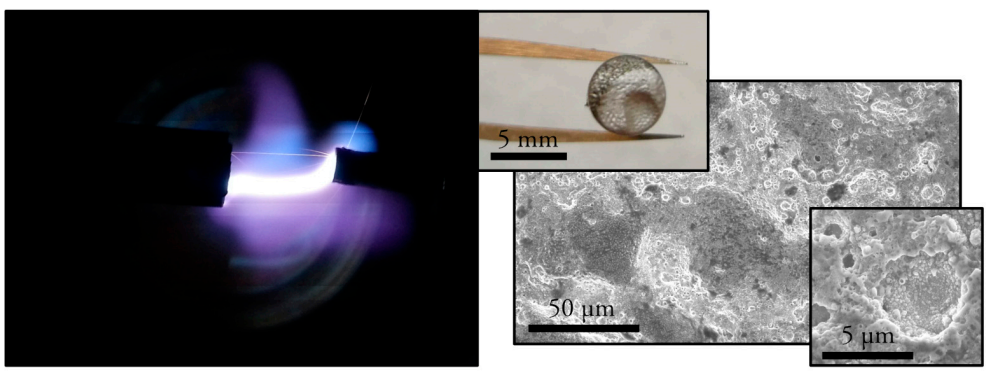

Figure 2.2. The photograph on the left shows the moment when the plasma is generated and a spark is generated between the electrodes. The sparks create both macroscopic craters in the electrodes visible with the naked eye, and microscopic craters visible with SEM (right).

The nanoparticle generation is mainly governed by the energy and the frequency of the sparks. The frequency of the sparks is directly proportional to the applied current, and inversely proportional to the discharge voltage. The energy, on the other hand, is proportional to the square root of the discharge voltage[61]. In other words, increasing the discharge voltage increases the energy of each spark, but the sparks are less frequent. The discharge voltage is therefore an important parameter that can sometimes be difficult to control. It depends on the type of carrier gas, the pressure in the system, and the distance between the electrodes[65]. If the electrodes are pointed and the energy of the sparks is high, the electrodes will slowly wear out. This causes the gap to increase, and in turn increasing the discharge voltage and the energy of the sparks. Since the ablated mass is directly proportional to the energy of the sparks[66], changes in the gap distance affect the stability of nanoparticle generation.

The local extreme heat created by the spark causes a supersaturated vapor plume of ablated material. The released particles have high energy, and high initial collision rate, due to the supersaturation. Small clusters nucleate and grow by complete coalescence when colliding with other particles. Heat is released at each collision due to the decreasing surface area of the particles, which increases the temperature of the particles and speeds up the coalescence[67–69]. As the particles grow, the released heat for each collision decreases. The time between each collision also decreases, and the cooling time of the particles increases. The particles continue to merge by complete coalescence until the collision time between the particles is longer than the cooling time. At this point, collisions are not followed by complete coalescence. Instead, the particles adhere, forming agglomerates composed of small primary particles[69]. The size of the primary particles varies between 2 and 10 nm[69], and depends on several parameters, such as the electrode material[70], rod diameter[71], and the characteristics of the spark[61]. The entire process from spark to vapor, and finally to the formation of agglomerates, is illustrated in Figure 2.3.

The concentration and size of the primary particles governs the rate of agglomeration. If the concentration of primary particles is high, and the gas flow rate low, large agglomerates are formed. Agglomeration can be avoided by increasing the carrier gas flow. The quenching rate then increases and the particles are more rapidly transported away from the heated zone, resulting in smaller primary particles with a lower probability of colliding[72,73]. This can also be achieved by locally increasing the gas velocity in the spark region. This can be performed by using alternative electrode configurations such as the pin-to-plate[74], or wire-in-hole[75]. These configurations have proven effective in the formation of sub-10 nm non-agglomerated nanoparticles. However, the rod-to-rod configuration is preferable when larger nanoparticles are desired, and it also has the advantage of being stable over long time[75].

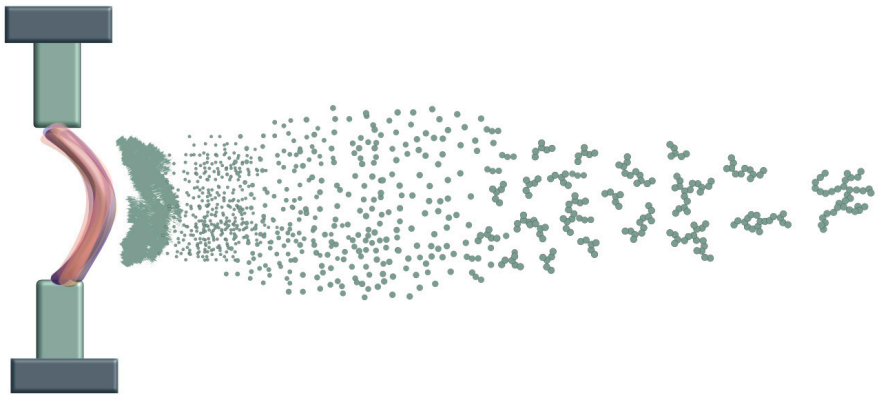

Figure 2.3. The formation of nanoparticles in the vicinity of the spark. The spark ablates material from the electrodes, and a metallic vapor is formed. Small clusters nucleate and grow by complete coalescence when colliding with other particles. The particles continue to collide and grow by complete coalescence until they reach a certain size, and become primary particles. Further collision events between the primary particles lead to the agglomeration.

Spark mixing

The high local temperature, supersaturation, and the rapid cooling of the vapor make spark ablation an ideal method for mixing materials to form multicomponent nanoparticles. Nanoparticles composed of materials that do not mix in bulk, so-called immiscible materials, have been generated by spark ablation[14]. This technique has also been used to form high-entropy multicomponent nanoparticles composed of up to six different elements[76]. Mixing components by spark ablation is simple, and can be achieved by using electrodes composed of different materials, or alloyed electrodes[14,77].

It is difficult to predict the composition of nanoparticles formed when using electrodes of different materials. The composition of the nanoparticles depends on the material properties, as well as which of the electrodes that initially acts as the cathode[70,78]. The heavier positive ions travel toward the negative cathode and cause stronger ablation, and more material is released compare to the positive anode[77]. The vapor and the atoms from the two electrodes can be successfully mixed because the ablated material travels as a jet between the two electrodes[65]. The drawback of this is that it might lead to redeposition of material on the opposite electrode, potentially causing the nanoparticle generation to become unstable, thus the nanoparticle composition may change with time.

Using alloyed electrodes allows more controlled particle composition as the problem of the greater ablation of the cathode is avoided. The atoms from the alloy are equally distributed in the metallic vapor and the agglomerates will have a similar composition to those of the electrodes[79,80]. *Paper I* describes a study in which alloyed electrodes with the composition $Fe_{82.5}Cr_{17.5}$ and $Fe_{85}Mn_{15}$ were used to form mixed nanoparticles in two different carrier gases. The different carrier gases were used to study the oxidation of the

nanoparticles, and this will be described more in detail in the next section. The composition of the individual nanoparticles was measured with x-ray energy-dispersive spectroscopy (XEDS) in scanning transmission electron microscopy (STEM) mode (see Appendix for technical details). Considering the transition metal elemental ratio, the composition of the resulting nanoparticles was almost identical to that of the electrodes for both alloys, even when generated with different carrier gases, see Table 2.1. This indicates that the use of alloyed electrodes is preferable if the purpose is to generate nanoparticles with a specific composition.

Table 2.1. Composition of the nanoparticles generated with pure N_2, or with a gas mixture of N_2 and 5 % H_2. The data are based on XEDS measurements of individual nanoparticles in STEM mode. The standard deviation (SD) is based on 25-40 measured nanoparticles for each system.

Electode/nanoparticle composition	Fe (at. %)	SD (at. %)
FeCr electrode	82.5	
FeCr nanoparticles generated with N_2	80	2
FeCr nanoparticles generated with N_2 + 5 % H_2	84	2
FeMn electrode	85	
FeMn nanoparticles generated with N_2	86	3
FeMn nanoparticles generated with N_2 + 5 % H_2	85	3

Oxidation

It may be difficult to avoid oxidation of the nanoparticles during aerosol generation. The aerosol in the work described here was generated at atmospheric pressure. Before the carrier gas is introduced into the system, and before the spark is running, the system is pumped down to a pressure of less than 10 mbar to remove impurities and oxygen. However, this is not sufficient for some materials that oxidize easily, and the small amounts of oxygen or water impurities remaining can cause the nanoparticles to oxidize.

It is possible to compare different elements and predict whether or not a nanoparticle composed of a certain element is expected to oxidize. Several types of nanoparticles were generated in this work: Fe, Cr, Mn, FeCr, FeMn (*Paper I*), Au, Bi, Cu (*Paper II*), Co, Ni (*Paper III*), CoPd, CoAu, and Pd (Chapter 5). The different elements can be compared by studying the Ellingham diagram of common oxidation reactions, to determine which are more likely to undergo oxidation. Of the elements studied here, the most likely to oxidize is Mn, followed by Cr and Fe, while Co, Cu, Ni, and Bi are much less likely to oxidize. The inert elements Au and Pd are not expected to undergo oxidation.

Oxidation takes place on the surface. For nanoparticles with a size similar to the mean free path of the gas, oxidation is governed by the collision of oxygen molecules, and the transport of these molecules through the metal oxide layer formed[81]. This transport is driven by the Cabrera–Mott model for low-temperature oxidation[82,83]. When oxygen

molecules are absorbed on the metal oxide surface, an internal electric field is created, which drives the diffusion of oxygen molecules through the metal oxide layer. As the metal oxide layer becomes thicker, the electric field strength is reduced, and the rate of diffusion of oxygen molecules decreases rapidly and thus so does the oxidation rate. For example, Fe nanoparticles in ambient air at room temperature would form a 1-nm thick metal oxide layer after 0.2 fs. The next nm would take 40 s to form, and the growth of a 3- and 4-nm thick metal oxide layer would take 40 weeks and 600 years, respectively[83]. This rapid change, where a thin oxide layer is formed instantly and then stops growing is referred to as self-passivation, and has been thoroughly studied in Fe nanoparticles[84–87].

Pure H_2 can be used as the carrier gas[88], or a small amount of H_2 can be added to N_2, to minimize the oxidation of the nanoparticles in the aerosol phase[89]. For elements that are likely to oxidize, such as Bi, Sn, and Co, a considerable difference can be observed in the resulting particles when using N_2 with H_2 as the carrier gas[89]. The effect of the carrier gas on the oxidation of alloyed FeCr and FeMn nanoparticles was studied (*Paper I*), and the results are shown in Figure 2.4. Transmission electron microscopy (TEM) images revealed a structural difference between nanoparticles generated with different carrier gases.

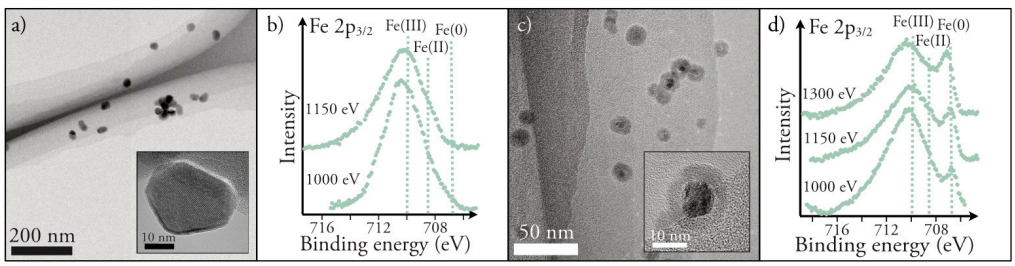

Figure 2.4. TEM images and XPS data from FeCr nanoparticles generated with a carrier gas composed of N_2 and N_2 + 5 % H_2. The nanoparticles generated with pure N_2 formed a single-phase, crystalline structure (a). The XPS measurements indicated only the presence of Fe-oxide and no metallic Fe(0) (b). The nanoparticles generated with a carrier gas of N_2 + 5 % H_2, formed a core-shell structure with a crystalline core and an amorphous shell (c). The XPS data show a clear metallic Fe(0) signal together with strong peaks indicating Fe oxides (d). This indicates that the nanoparticles formed are self-passivated nanoparticles.

The nanoparticles generated with pure N_2 had a single crystalline phase, whereas those nanoparticles generated with a gas mixture of N_2 + 5 % H_2 had a core-shell structure (Figure 2.4a,c). X-ray photoemission spectroscopy (XPS) measurements of the Fe $2p_{3/2}$ spectra revealed a pure Fe(0) signal in the core-shell nanoparticles, but not in the nanoparticles generated without H_2 (Figure 2.4b,d). The addition of H_2 prevents the primary particles and agglomerates from oxidizing and a stable non-oxidized core may form before the particles are oxidized. The core-shell structure formed is the result of self-passivation of the Fe-based nanoparticles. The self-passivated core-shell nanoparticles

revealed no significant difference in shell thickness when they were studied again one year later. Furthermore, the shell had a similar thickness, regardless of the size of the nanoparticles in the range from 15 to 40 nm. In contrast, the nanoparticles generated without H_2, were probably oxidized before compaction, and the resulting compacted nanoparticles were completely oxidized.

Compaction

As described above, the formation of agglomerates is common when generating nanoparticles by spark ablation. However, this is undesirable in some applications, where compact monodisperse nanoparticles are required. Irregularly shaped agglomerates can be transformed into more compact shapes by in-flight reshaping in a high-temperature tube furnace.

The compaction mechanism of agglomerates takes place in several stages. When heated, the neck region between two adjacent primary particles increases, causing the primary particles to grow. Whether this is due to atom migration on the surface, or evaporation and condensation in the neck region, is not known, however, according to the Kelvin equation it is expected that the primary particles will evaporate at sintering temperatures[90]. The growth of the primary particles and the neck region causes densification of the entire agglomerate, and the mobility diameter decreases (Figure 2.5)[91–93]. This continues until densification and compaction are complete, and ideally a spherical nanoparticle is formed. If the structure is heated further, internal restructuring occurs, and later the nanoparticle starts to evaporate[91,94,95].

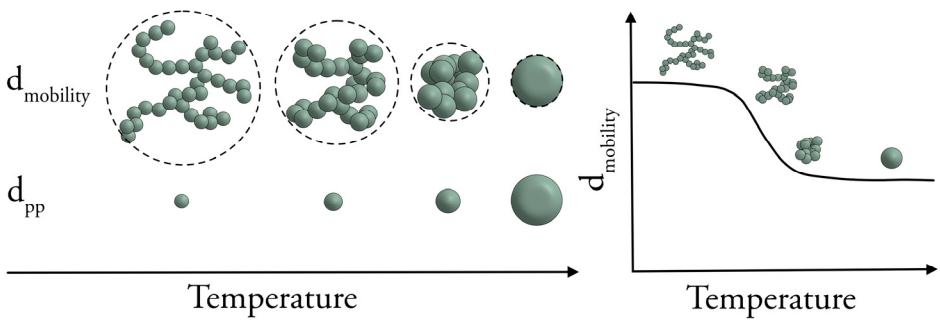

Figure 2.5. The transformation of agglomerates into compact nanoparticles. With increasing temperature, the agglomerates become more compact, and the mobility diameter of the agglomerates decreases. At the same time the primary particles in the agglomerates grow, due to sintering. A compaction curve is obtained by plotting the mobility diameter against the temperature. Initially the agglomerates are unaffected by the increased temperature and the mobility diameter remains constant. As the agglomerates start to compact, the mobility diameter decreases and this continues until the nanoparticles are compacted and no further decrease in mobility diameter is observed.

The temperature, at which the compaction is initiated depends on the size of the primary particles, as well as the composition of the agglomerates[96]. Oxygen or other impurities on the surface of the agglomerates generally suppress compaction, increasing the temperature at which the agglomerates starts to compact[92,97]. If the size and composition of the primary particles are identical, the number of primary particles in the agglomerates would not affect this onset temperature. However, the temperature at which the compaction is completed depends on the number of primary particles in the agglomerates[91,96]. The temperature at which the mobility diameter stops decreasing and the nanoparticles start to undergo internal restructuring, is called the compaction temperature (T_C). As a rule, this temperature varies between 30 and 50 % of the bulk melting temperature in Kelvin (T_M). If the agglomerates are oxidized, the value will be closer to 75 % of T_M[97].

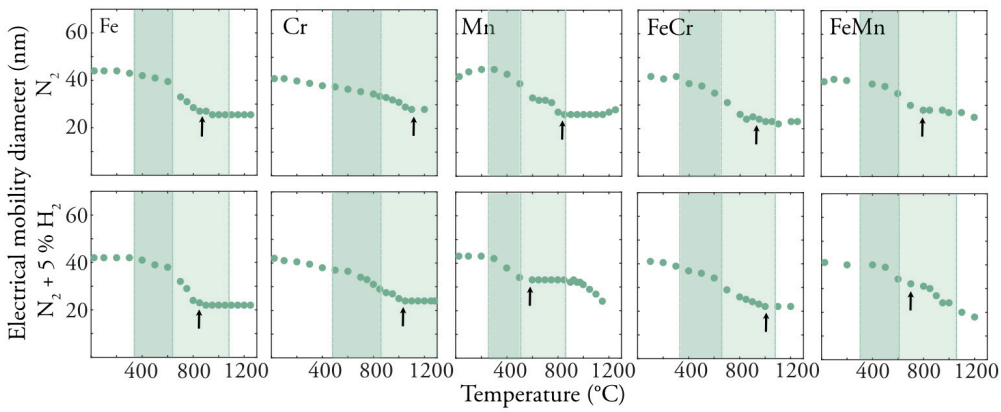

Figure 2.6. Compaction of Fe, Cr, Mn, and the mixed FeCr and FeMn nanoparticles with two different carrier gases (N_2 and N_2 + 5 % H_2) was studied. The estimated compaction temperatures based on the appearance of the compaction curves are indicated by the black arrows. The region between 33 % and 50 % of the bulk material melting temperature in Kelvin is shaded in darker green, and the region between 50 % and 75 % of the bulk melting temperature is shaded in lighter green.

The compaction of Fe, Cr, and Mn and their mixed combinations was studied with two different carrier gases, N_2 and N_2 + 5 % H_2 (*Paper I*). The results are shown in Figure 2.6. The data were collected from tandem DMA measurements. Each data point was acquired by size-selecting agglomerates with the first DMA, and then measuring with the second DMA how the mobility diameters changed after the agglomerates were heated in the tube furnace. The estimated values of T_C are indicated by the black arrows, and 33, 50 and 75 % of T_M are indicated in the figures. In all cases, T_C was determined to be between 50 and 75 % of T_M. The difference between the two gases is small for most systems, with a slight tendency for T_C to be higher for nanoparticles generated without H_2.

Evaporation

At the compaction temperature, densification cease, and the nanoparticles undergo internal restructuring. This is seen by the flattening out of the curves in Figure 2.6. If the temperature is further increased, the nanoparticles start to slowly evaporate, which is seen as a second slope in the electrical mobility diameter. The evaporation of nanoparticles is governed by vapor pressure, and occurs at lower temperatures than the bulk boiling temperature of the material. Figure 2.7a shows vapor pressure curves for some metallic elements[98]. A high vapor pressure indicates that an element is more likely to evaporate. It can be seen in this figure that the vapor pressures for Fe, Cr, and Co are similar, whereas the vapor pressures for Mn and Bi are much higher. It has been estimated that 50 nm Bi nanoparticles would start to evaporate at about 600 °C[99]. The vapor pressure of nanoparticles is affected by the Kelvin effect, i.e., smaller particles with a larger curvature have an increased tendency to evaporate. It has been shown that the evaporation temperature (T_E) of PbS nanoparticles is shifted by 100 °C when the size of the nanoparticles was decreased from 20 nm to 10 nm[90].

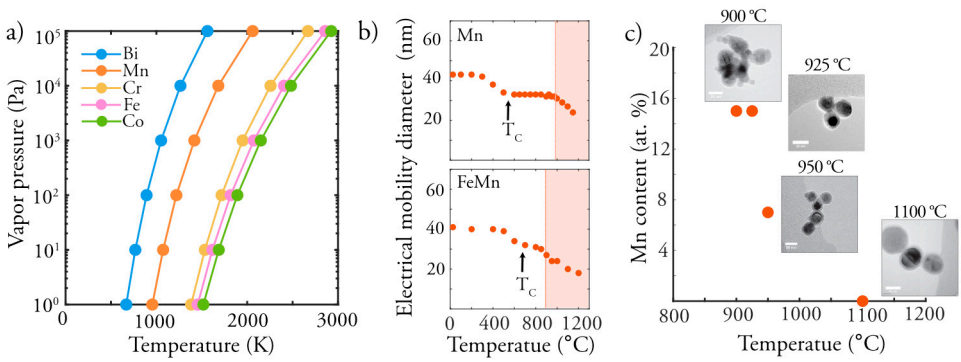

Figure 2.7. Vapor pressure curves for different elements extrapolated from CRC Handbook of Chemistry and Physics[98] (a). Compaction curves for Mn and FeMn with the compaction temperature (T_C) marked with black arrows, and the estimated regime for evaporation marked in shaded red (b). The content of Mn in FeMn with increasing temperature (c). Mn starts to evaporate from the FeMn nanoparticles at about 950 °C.

When studying the compaction behavior of the different nanoparticle systems in Figure 2.6, a second slope, indicating evaporation, is observed at about 1000 °C for Mn and at about 900 °C for FeMn when using the gas mixture of N_2 + 5 % H_2. This is visualized in Figure 2.7b where T_C and the regime for evaporation are indicated based on the compaction behavior. To confirm that the observations can be attributed to the evaporation of Mn, FeMn alloyed nanoparticles generated at four different temperatures were investigated with XEDS (Figure 2.7c). At 900 °C, the average atomic percent (at. %) of Mn in the nanoparticles was 15 at. %, which is in agreement with the composition of

the electrodes. The same result was obtained for nanoparticles generated at 925 °C. However at 950 °C, the composition of Mn in the nanoparticles started to change. Some of the nanoparticles were still composed of 15 at. % Mn, while others had a much lower Mn content. No Mn was detected in the nanoparticles generated at 1100 °C, indicating that the Mn had evaporated from the FeMn nanoparticles. It should also be noted that FeMn nanoparticles generated without H_2 and heated at 1100 °C still contained of 15 at. % Mn. The nanoparticles generated with H_2 thus appeared to be more prone to evaporation, and oxidation might prevent evaporation.

Thermal charging

Size-selection in a DMA is based on the electrical mobility of the nanoparticles, and the nanoparticles are assumed to carry a single charge. However, if the nanoparticles are heated, additional thermal charges may be added to the nanoparticles, which will affect the measured size distribution. Each data point in Figure 2.6 was acquired from a DMA scan in which the peak value of each size distribution was analyzed. This can also be displayed by superimposing the scans on top of each other, as in Figure 2.8. The size distribution typically follow a log-normal distribution, but at high temperatures the measured size distribution shows a bi- or trimodal distribution, which indicates that the nanoparticles carry more than one charge.

A bimodal size distribution was observed at about 1000 °C for Cr and Mn with both types of carrier gas (see Figure 2.8a-d). The greatest difference between these systems was found when comparing Cr in different gases. The size distribution for Cr generated with a carrier gas containing 5 % H_2 at 1200 °C is shifted to smaller nanoparticle sizes, possibly due to large number of multiply charged nanoparticles. Fe nanoparticles carry more than two charges at high temperatures. The highest number of charges was found at 1100 °C. Above this temperature, most of the additional charges seem to disappear, and for the nanoparticles generated in N_2 at 1250 °C, only the single charge peak is observed. For nanoparticles generated at the same temperature in the carrier gas with H_2, most of those carrying four or five charges had disappeared, while peaks indicating one to three charges were still visible.

Based on these results, it appears that the thermal charging of the nanoparticles is dependent on both the carrier gas and the nanoparticle composition. As discussed above, the carrier gas affects oxidation, and perhaps also the surface properties of the nanoparticles. This might also influence the probability of a nanoparticle to gain additional charges. It is interesting to note that charging seems to take place within a certain temperature interval, where the largest number of charges is seen at about 1100 °C. Above 1200 °C the particle distribution returns to a single peak, indicating only

singly charged nanoparticles. The particle concentration also appears to be much lower at this point. Similar behavior has been reported for compacted 20 nm Au particles. In that case, multiply charging was observed in the region between 600 and 1300 °C, while above this, the charged particles disappeared[100]. Thermal charging during compaction is an interesting and well-known phenomenon[101–103] which, unfortunately, reduces the quality of particle generation. Thermally charged particles destroy the monodispersivity, since larger multiply charged particles also pass through the DMA during size-selection.

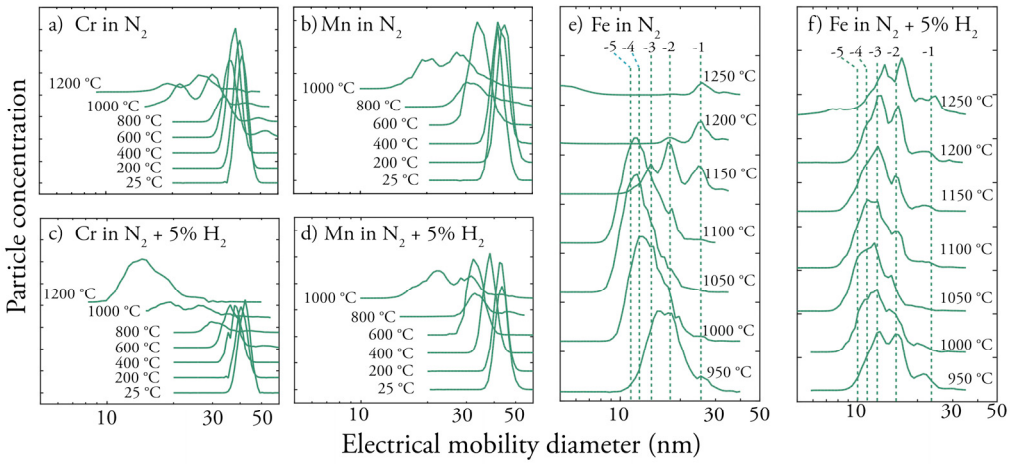

Figure 2.8. The particle size distributions of Cr, Mn, and Fe generated at different temperatures and in different carrier gases. The shifting of the peaks toward smaller particle diameters with increasing temperature is expected due to the compaction of the agglomerates. A bimodal size distribution is observed at around 1000 °C for Cr and Mn due to thermal charging of the nanoparticles (a-d). The Fe nanoparticles become multiply charged, with five or more charges (e-f). Charging appears to take place within a certain temperature interval, above which the number of additional charges decreased.

Deposition

The final stage of aerosol generation is the collection or the deposition of the nanoparticles. During this step, the nanoparticles are extracted from the carrier gas and directed towards a substrate for post-generation characterization. This has been studied in great detail in the present work, and two entire chapters are dedicated to this. The first, Chapter 3, describes the deposition of a collection of particles in an ESP from a macroscopic point of view, whereas the second, Chapter 4, deals with the deposition of individual nanoparticles from a microscopic point of view.

3. The collection of aerosol nanoparticles

The phenomenon of collecting of charged aerosol particles using electric fields by electrostatic precipitation has been known for a long time. The first ESP was developed more than 100 years ago for the purpose of controlling and removing dust from industrial plants to avoid air pollution[104]. The removal of particulate matter using this technique has been refined since then, and ESPs are nowadays commonly used in combination with particle filters, for example, to eliminate mercury emissions from coal-fired power plants[105,106]. ESPs can also be used to remove airborne viruses[107,108].

ESPs are not only effective in cleaning air. They can also be used to sample aerosol particles for *ex situ* characterization, or to collect them for other applications. Capturing aerosol particles and transporting them to a substrate is therefore an essential part of the aerosol generation process. An ESP was used in the present work to deposit nanoparticles onto substrates, and such an ESP is described in detail in this chapter. The parameters governing the deposition in an ESP are also thoroughly discussed.

Electrical mobility

To capture aerosol particles with an ESP, they must be positively or negatively charged. Charged particles placed in electric field are exposed to a constant electric force. The efficiency of an ESP is largely dependent on the electrical mobility of the charged particles in the gas flow when exposed to this constant electric force.

In this chapter, all particles considered are smaller than 100 nm. Much of the dynamics governing the movement of larger macroscopical particles is also valid for nanoparticles, however, a few additional factors have to be considered. Nanoparticles are considered to be in the free-molecular regime, in which they are affected by the individual molecules in the surrounding gas[109]. The gravitational force is considered negligible in the gas, and the nanoparticles do not sediment. Instead, they are carried by the gas, and follow the same trajectory as the gas flow due to the drag force (F_D) given by the following equation:

$$F_{\mathrm{D}} = \frac{3\pi\eta d_{\mathrm{p}} v}{C_{\mathrm{c}}} \tag{3.1}$$

where η is the viscosity of the gas, v is the particle velocity, d_{p} is the particle diameter and C_{c} is the Cunningham slip correction factor. This factor takes into account how much faster than expected a particle settles when avoiding collisions with gas molecules. The correction factor for larger particles is unity, since they cannot avoid the gas molecules, and are thus not expected to settle faster. For smaller particles, that can avoid gas molecule collisions, C_{c} is higher.

Inside the ESP, particles with a charge (q) are exposed to an electric field (E). The electrostatic force (F_{E}) acting on these particles, due to the electric field, is given by the following relation,

$$F_{\mathrm{E}} = qE. \tag{3.2}$$

The electrical mobility (Z) of the particles is defined by assuming $F_{\mathrm{D}} = F_{\mathrm{E}}$, and denoting the drift velocity of the particles in the electric field as v_{d},

$$Z = \frac{v_{\mathrm{d}}}{E} = \frac{neC_{\mathrm{c}}}{3\pi\eta d_{\mathrm{p}}}. \tag{3.3}$$

The electrical mobility of a particle is an important parameter in aerosol physics, since many aerosol instruments rely on it. The electrical mobility and drift velocity are also important for particle collection and deposition in an ESP, as will be discussed later in this chapter.

ESP for nanoparticle collection

As the field of aerosol science and technology has developed, so have specialized ESPs for nanoparticle deposition. A reliable method is required for the collection of nanoparticles on a flat surface in order to be able to thoroughly characterize the size, shape, and functionality of engineered nanoparticles. In 1967, Liu et al. developed a two-stage parallel-plate ESP to capture particles on a flat surface for microscopy studies[110]. In their setup, the gas flowed parallel to the precipitation zone, where an electrical potential was applied. They were able to demonstrate high collection efficiency and good deposition uniformity compared to previously developed ESPs. However, the sampling efficiency was dependent on the particle size, and the efficiency was much lower for small

nanoparticles[110]. Many years later, Dixkens and Fissan described a new type of ESP, which, in contrast to previous ESPs, demonstrated a collection efficiency of 100 % for particles smaller than 100 nm[39]. This type of ESP is now commercially available, e.g. the TSI 3089 and Grimm 5561 models, and is also the type of ESP used in the present work.

The Dixkens and Fissan ESP

The Dixkens and Fissan type ESP, with the geometric dimensions used in the present work is illustrated in Figure 3.1a. The aerosol enters the ESP from above, and follows the gas flow trajectory towards the collection plate. As the gas flow reaches the plate, the direction of the flow changes and the gas flows parallel to the collection plate. The gas flow profile and streamlines obtained from COMSOL Multiphysics simulations are shown as colored profiles in Figure 3.1b-c. A high electric potential is applied to the collection plate, creating a homogeneous electric field between the collection plate and the grounded walls. The strength of this electric field depends on the applied potential (ϕ) and the distance (h) between the inlet and the collection plate. The charged particles are constantly exposed to an electrostatic force oriented perpendicular to the collection plate. This electrostatic force draws the particles away from the gas, towards the collection plate, and when the particles reach the plate, they stick and are collected.

Dixkens and Fissan reported that all the deposited particles were collected within a circular spot, and that the particle concentration profile inside the spot was homogeneous. The particle concentration profile follows a so-called top-hat profile, with constant concentration within the spot, and sharp edges with no deposited particles outside the spot. However, they did not derive the exact relation between the deposition parameters and the size of the deposition spot. Other researchers later pointed out that the size of the spot depends on a number of key variables, but did not present the exact relation[111,112]. Without knowing this relation exactly, it is impossible to predict the particle concentration on the substrate without performing off-line analyses. Also, if this relation were known, it should be possible to fine-tune the spot size in order to minimize the deposition time, and to ensure that the entire substrate is covered with particles. The exact relation between the deposition variables and the deposition spot size was derived in this work (*Paper II*).

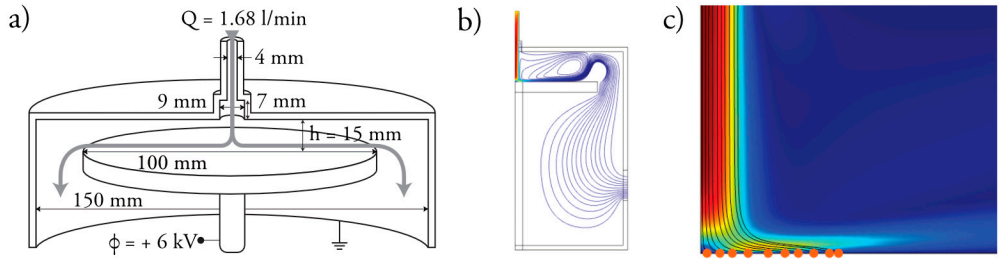

Figure 3.1. Schematic of the ESP used in this work with the standard geometric dimensions (a). The aerosol enters from above and the particles are deposited onto the collection plate. Gas flow simulations performed with COMSOL Multiphysics showing the gas streamlines in the ESP (b). The ESP chamber was simulated in 2D and viewed from the side. Due to axial symmetry, only one side was modelled. The particle trajectories (black lines) and their end positions (orange circles) are shown together with the gas flow velocity (colored profile) in the upper part of the ESP, close to the collection plate (c). The particles are equally distributed, and the distance from the center to the last deposited particle gives the radius of the deposition spot.

Deposition in an ESP

Using COMSOL Multiphysics to model particle deposition in an ESP

The deposition in an ESP was modelled using COMSOL Multiphysics. COMSOL Multiphysics is a finite-element software, in which the behavior of heat, fluids, electrostatics etc. is solved in different scenarios by partial differential equations. To model the deposition of nanoparticles in an ESP, three modules were used to cover the relevant physics. First, the fluid dynamics was modelled. The gas was considered to be laminar and incompressible, and its dynamics solved with the Navier–Stokes equation. Next, the electrostatic forces were modelled. To do this, a constant electrical potential was set to the deposition plate, and the surrounding walls were grounded. The solution was obtained from Gauss's law for the electric field. Finally, the particle trajectories were determined. This was done using input from the first two modules and the trajectories were calculated using Newtonian mechanics,

$$m_{\mathrm{p}} \frac{dv_{\mathrm{p}}}{dt} = F_{\mathrm{D}} + F_{\mathrm{E}} + F_{\mathrm{B}} \tag{3.4}$$

where F_{D} is the drag force, F_{E} is the electrostatic force, and F_{B} is the force due to Brownian motion. To reduce the level of complexity of the simulations, and the computational time, a 2D model of the ESP was constructed for the calculations, and since the chamber has axial symmetry, only one side of the ESP was modelled, as shown in Figure 3.1b-c.

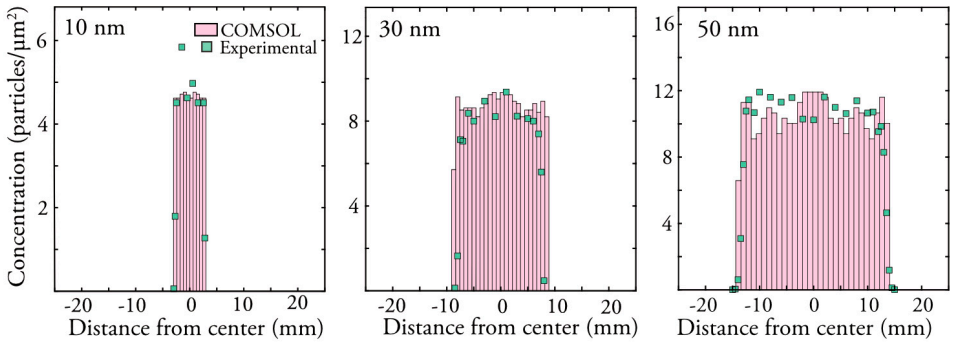

Figure 3.2. Comparison of the results of COMSOL Multiphysics simulations (pink bars) and experimental data (green squares) for the deposition of 10, 30, and 50 nm particles. In all cases the simulated and experimental depositions followed similar top-hat profiles, with a high homogeneous concentration inside the spot and no particles deposited outside this area. The particle concentration on the y-axis is the experimentally determined concentration. Each simulation included 1000 monodisperse nanoparticles.

COMSOL Multiphysics simulations were comparted with experimental results using different nanoparticles sizes (10, 30, and 50 nm) to evaluate the deposited particle concentration profiles and the spot size. The deposited particle concentration was determined from SEM analysis, and the results are shown in Figure 3.2. From the simulations and the experimental data, it was concluded that the particle concentration follows the previously reported top-hat profile, with high, constant concentration within the spot, and with no particles being deposited outside the spot. A slight tail was observed for the experimental data, and this might be due to the slightly non-monodisperse size distribution that results from size-selection in a DMA[113]. The simulations and the experimental data showed very similar sizes of the spot for the different particle sizes, indicating that COMSOL Multiphysics is a valid method for studying nanoparticle deposition in an ESP.

Results from COMSOL Multiphysics simulations revealed that Brownian motion had little or no influence on the spot size (Figure 3.3). Brownian motion is the small displacement, or random motion, resulting from collisions between the particles in the gas and the surrounding gas molecules. This displacement is larger for smaller particles and affects the final position of a single nanoparticle in the gas. The nanoparticles are typically inside the ESP for about 1 s, and during this time, the displacement due to Brownian motion is on the order of 0.01-0.1 mm[1]. The deposition spot size is governed by the collective behavior of the aerosol, and ranges from a few mm to tens of mm. The spot size is therefore much larger than the displacement of individual nanoparticles, and Brownian motion thus has a negligible influence on the spot size.

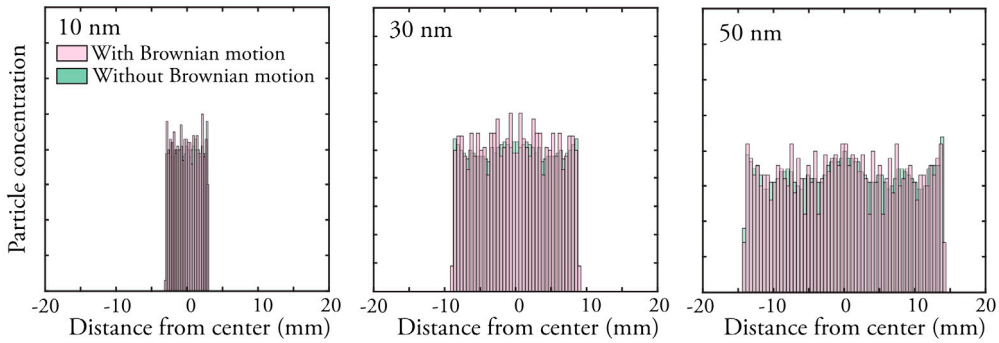

Figure 3.3. Results of COMSOL Multiphysics simulations with Brownian motion (pink bars) and without Brownian motion (green bars). The spot radius was unaffected by the inclusion of Brownian motion for all three particle sizes (10, 30, and 50 nm).

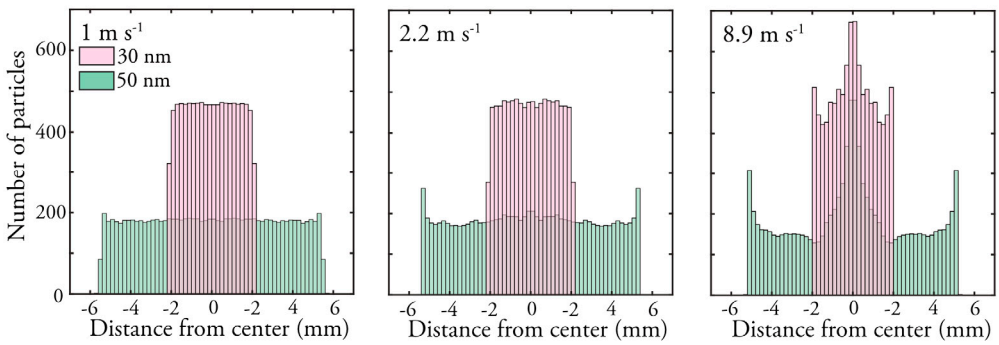

Figure 3.4. Effects of varying the gas velocity in the inlet tube. When reducing the gas velocity both the spot size and particle concentration profile remained the same. When the gas velocity was increased, a large number of particles were deposited in the center and at the edges, and the profile no longer had a top-hat profile, however, it should be noted that the spot size is almost unaffected by this increased gas velocity.

The influence of the gas velocity was also investigated by keeping the gas flow rate constant while changing the radius of the inlet tube for 30 and 50 nm particles. When increasing the inlet diameter, and thereby lowering the gas velocity to less than 1 m s^{-1}, the spot diameter remained constant, as did the particle concentration profile. However, when the radius of the inlet tube was decreased, thus increasing the gas velocity, the particle concentration profile changed (Figure 3.4). Instead of the characteristic top-hat profile, an increase in particle concentration was observed in the center of the spot and at the edges.

The increased concentration in the center is most likely due to the impaction of particles with a high velocity in the center. Unexpectedly, the spot size was almost unaffected by this change in the particle concentration profile. This might be due to the low gas velocity

close to the walls in the tube. In a laminar gas flow, the gas profile in the tube follows a parabolic function with the highest velocity at the center, and zero gas velocity close to the walls. The particles deposited close to the edges of the spot are also transported close to the walls in the inlet tube. These particles have a too low initial gas velocity to be affected by an increase in velocity, and are therefore deposited at a similar position, regardless of any increase in gas velocity.

Variables affecting the spot size

The COMSOL Multiphysics simulations revealed that only four variables had a significant influence on the deposition spot size. The gas flow rate (Q) and the distance between the inlet and the plate (h) exhibited an almost perfect square root dependence, whereas the applied electrical potential (ϕ) and the particle electrical mobility (Z) showed an inverse square root dependence, as can be seen in Figure 3.5a-d.

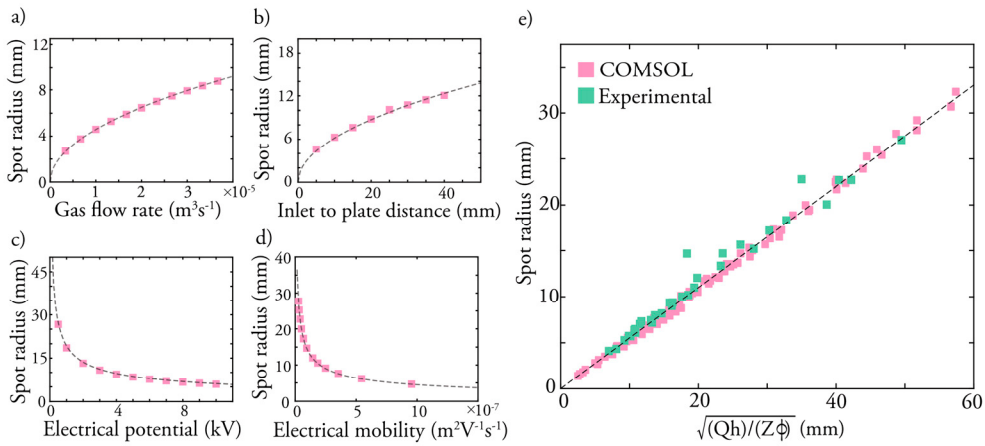

Figure 3.5. The spot radius exhibited a square root dependence on the gas flow rate and the distance between the inlet and the plate (a-b). The electrical potential and the particle electrical mobility showed inverse square root dependence (c-d). These results were combined into a semi-empirical equation. The spot radii obtained from experimental measurements of the depositions (green squares) and simulations (pink squares) are plotted against the relations found in *a-d* (e). The data points followed a linear relation, and the constant κ was determined from the linear fit to be 0.55.

The following semi-empirical formula was obtained, explaining the dependence of the radius of the spot on these four variables:

$$r_{\text{spot}} = \kappa \sqrt{\left(\frac{Qh}{Z\phi}\right)} \tag{3.5}$$

where κ is a dimensionless constant when all other variables are expressed in standard units. The value of κ is determined from the linear fit obtained when plotting the spot radius against the expression using experimental data points and the results from COMSOL Multiphysics simulations (Figure 3.5e). From the linear fit, κ was determined to be 0.55, which is nearly identical to $\sqrt{1/\pi}$. This expression can thus be rewritten as below,

$$r_{\text{spot}} = \sqrt{\left(\frac{Qh}{\pi Z \phi}\right)}. \tag{3.6}$$

Significance of this new formula

Using the formula presented above, the radius of the spot can be predicted or fine-tuned by simply altering any of the four variables. However, the formula can be simplified further. Since $h/\phi = 1/E$, and $EZ = v_{\text{d}}$, the formula can be rewritten in the following form

$$r_{\text{spot}} = \sqrt{\frac{Q}{\pi v_{\text{d}}}}, \tag{3.7}$$

and the area of the spot (A_{spot}) can thus be expressed as

$$A_{\text{spot}} = \frac{Q}{v_{\text{d}}}. \tag{3.8}$$

The above expression reveals that the area of the spot depends only on the incoming gas flow rate and the drift velocity (v_{d}) of the particles in the electric field.

For deposition in an ESP using monodisperse particles, and with 100 % collection efficiency, the particle concentration inside the deposition spot can be predicted by simply dividing the total number of particles deposited by the area of the deposition spot,

$$c_{\text{spot}} = \frac{Qtc_{\text{gas}}}{A_{\text{spot}}}. \tag{3.9}$$

Replacing A_{spot} with the expression attained in Eq. 3.8, gives the following relation,

$$c_{\text{spot}} = t c_{\text{gas}} v_{\text{d}}. \tag{3.10}$$

In its final form, the concentration of particles inside the spot depends only on the deposition time (t), the particle concentration in the gas (c_{gas}), and the drift velocity of the particles in the electric field (v_{d}). Remarkably, this result implies that the concentration of particles inside the spot is independent of the gas flow rate. It is therefore only necessary to control the gas flow rate when a certain spot size is required, but not when determining the particle concentration inside the spot. This further implies that it should be possible to split the gas flow into multiple channels to perform multiple depositions, and each channel yields the same deposited particle concentration as from a single deposition.

The ability to predict the deposited nanoparticle concentration on the substrate using the proposed equations derived above is used frequently in the next two chapters. It is important to know the deposited nanoparticle concentration in order to study and compare the tendency to self-assemble, and this can be very difficult to determine from off-line analysis.

4. Self-assembly of magnetic aerosol nanoparticles

Self-assembly is a broad concept, ranging from the organization of atoms to that of galaxies[114]. The concept of self-assembly describes a process in which a system is reorganized into a more ordered structure, usually to reduce its free energy and reach thermodynamic equilibrium. When self-assembly occurs without any influence from the surrounding environment, it is referred to as *static*, and examples of this are when atoms arrange to form crystals, or when lipids organize into micelles[114]. When self-assembly is aided by the surrounding environment, it is called *directed* self-assembly, and can be achieved, for example, by applying templates or using external fields[115]. Magnetic objects experience a strong dipole – dipole interaction, and tend to self-assemble when placed in a magnetic field. Magnetic nanoparticles also self-assemble in the presence of a magnetic field, usually into chain-like structures[46,48,116,117].

This chapter describes how directed self-assembly can be applied when depositing aerosolized magnetic nanoparticles. In the first part of the chapter, the most important aspects of magnetism and magnetic nanoparticles are described. The second part is based on the results presented in *Paper III*, where it was described how the self-assembly of magnetic aerosol nanoparticles can be directed in a combined electric and magnetic field.

Magnetic nanoparticles

Magnetic nanoparticles are a popular topic of study, and are commonly used in biomedical applications such as bioimaging[118], cancer treatment[119,120], and drug delivery[121]. Magnetic nanoparticles have also shown potential in solid-state applications such as high-density magnetic storage and high-performance permanent magnets[122,123]. This chapter focuses on the formation of nanostructures using self-assembled magnetic nanoparticles. A basic understanding of magnetism and magnetic nanoparticles is required to fully describe the mechanics of the magnetic-field-directed self-assembly.

Magnetism

According to one of Maxwell's equations on electromagnetism, magnetic charges or magnetic monopoles cannot exist. The magnetic moment always points from the south pole to the north pole, generating a magnetic field that surrounds the body in a closed loop and forms a magnetic dipole. The direction of the magnetic field is always from the north towards the south (Figure 4.1a). When two magnetic dipoles are close to each other, they experience a dipole – dipole interaction, which depends on how the dipoles are oriented in space. Magnetic dipoles, such as magnetic beads thus spontaneously order themselves into a north-to-south configuration if placed close to each other. Later in this chapter, this type of self-assembly is exemplified by the formation of nanochains comprised of magnetic nanoparticles.

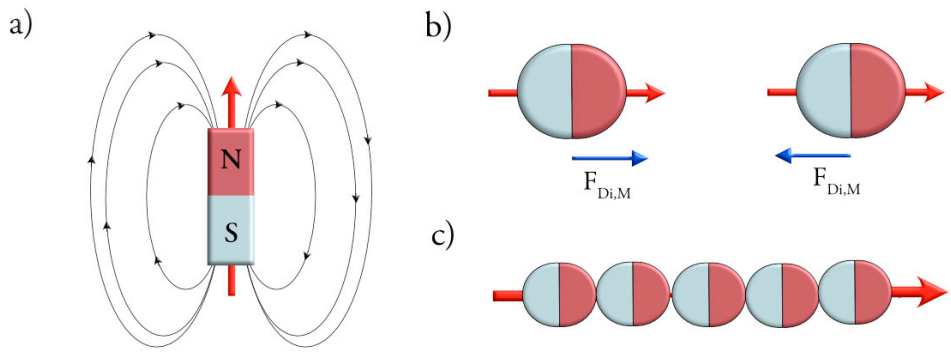

Figure 4.1. The magnetic moment always point from the south pole to the north pole, forming a magnetic field that surrounds the object (a). Two magnetic dipoles close to each other experience a magnetic dipole – dipole interaction (b), which forcing them to self-assemble into a north-to-south configuration (c).

Different materials experience different types of magnetism. Among the elements in the periodic table, in bulk form, the most common types of magnetism are: diamagnetism, paramagnetism, and ferromagnetism. Most elements in the periodic table are either diamagnetic or paramagnetic. The diamagnetic elements are usually referred to as non-magnetic, as they are not attracted by a magnetic field. When a paramagnetic material is exposed to an applied magnetic field, the atomic magnetic moments become aligned, but thermal energy causes the direction of the magnetic moments to fluctuate. If the external magnetic field is strong enough, or if the temperature is low enough, the magnetic moments retain their alignment and the material reaches saturation. However, if the magnetic field is removed, or the temperature increased, thermal energy causes the moments to become disordered again, resulting in no net magnetization. A ferromagnetic material, on the other hand, can easily be magnetized, and its magnetization is preserved

when the applied magnetic field is removed. Only three elements are ferromagnetic at room temperature (i.e., 300 K): Ni, Co, and Fe.

In this work, ferromagnetic nanoparticles at room temperature were mainly studied. The magnetization of a ferromagnetic material, when exposed to an applied magnetic field follows a so-called hysteresis curve. A hysteresis curve is obtained by plotting the magnetization (M) against the applied magnetic field (H), as illustrated in Figure 4.2a. A ferromagnetic material, starting from a demagnetized state, reaches its saturation magnetization (M_S) when exposed to a strong magnetic field (*i*). All the magnetic moments in the object are then aligned in the same direction, and increasing the magnetic field further does not increase the magnetization. The saturation magnetization depends on the material, and values for the three ferromagnetic elements can be found in Table 4.1. If the applied magnetic field is removed from the saturated material, its magnetization is preserved and this is called the remanent magnetization (*ii*). The magnetization becomes zero when the magnetic field is applied in the opposite direction to the initial direction (*iii*). The magnetic field required to reach this point is called the coercivity, and describes the material's resistance to demagnetization. Upon further increasing the applied magnetic field, the magnetic moments in the system become aligned reaching saturation again, but now in the opposite direction (*iv*).

From macroscale to nanoscale

New phenomena can occur on the nanoscale, and many properties may be different from those of bulk material, including the magnetic properties. The magnetic coercivity is highly dependent on the size of the system, as illustrated in Figure 4.2b. Ferromagnetic nanoparticles transform into a superparamagnetic state if the nanoparticles are sufficiently small. At room temperature, thermal energy overcomes the energy barrier that keeps the magnetic moments aligned, causing the direction of the magnetization to fluctuate, resulting in zero remanent magnetization. Whether or not a collection of nanoparticles is in a superparamagnetic state depends on the surrounding environment, including the temperature and interparticle interactions, as well as the particle size and the acquisition time of the measurement. It is therefore difficult to define at which size nanoparticles transform into a superparamagnetic state[124].

Table 4.1. Magnetic properties of the ferromagnetic elements in room temperature (i.e., 300K) with reported critical size of the single-domain.

	Saturation magnetization (emu/cm^3)	Single-domain size (nm)
Ni	485[125]	55[126], 82[127]
Co	1400[125]	60[127], 70[124,126]
Fe	1700[125]	14[126], 30[124]

A bulk ferromagnetic material is composed of many small magnetic domains, while a superparamagnetic nanoparticle is only composed of a magnetic single-domain. For single-domain particles, the size of the magnetic domain increases with increasing size of the nanoparticle. As the size of the nanoparticle and the magnetic domain increases, the magnetic single-domain becomes more stable, and the superparamagnetic nanoparticle transforms into a ferromagnetic state, and the coercivity increases[128]. This continues until it becomes more energetically favorable for the magnetic domain to split into smaller domains, which then reduce the coercivity. The critical size of the magnetic single-domain for the three different ferromagnetic elements can be found in Table 4.1

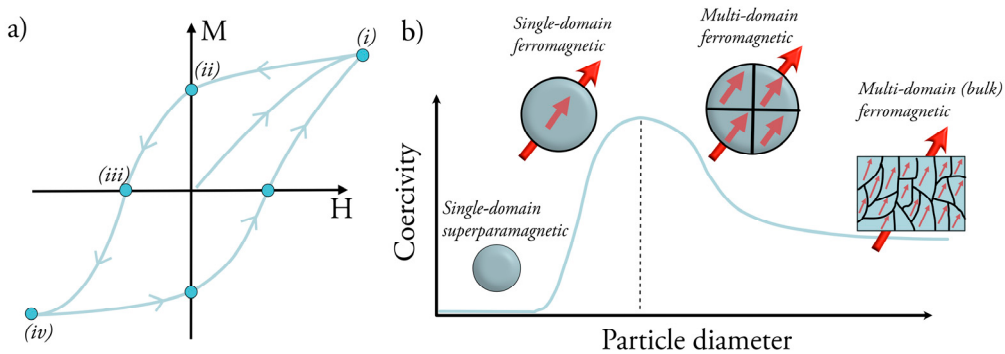

Figure 4.2. Hysteresis curve for a ferromagnetic material (a). Coercivity as a function of particle diameter close to the critical size of a magnetic single-domain (b). Small single-domain particles are superparamagnetic with zero coercivity and remanent magnetization. The magnetic single-domain becomes stable upon increasing the size of the particle, and the coercivity increases and reaches a maximum just before the single-domain splits into smaller magnetic domains.

Magnetic-field-assisted deposition

Ferromagnetic nanoparticles experience a strong dipole – dipole interaction and are expected to self-assemble. To study the self-assembly of magnetic nanoparticles and the influence of an applied magnetic field, it is important to bring the nanoparticles close to each other in a controllable way. This can be achieved by depositing aerosol nanoparticles in a magnetic-field-assisted ESP (MESP).

Magnetic-field-assisted ESP

The magnetic force acting on an object in a magnetic field is dependent on the gradient of the magnetic field and on the volume and saturation magnetization of the object. Larger µm-sized aerosol particles can thus be captured and separated in a gas flow by applying a strong magnetic field[129], and particles larger than 100 nm can be separated

using specialized magnetic filters[130–132]. It is much more difficult to capture particles smaller than 100 nm using of a magnetic field alone[130]. When separating small superparamagnetic nanoparticles in a solution, the applied magnetic field aligns the magnetization of the nanoparticles and induces a small motion. This small motion is not sufficient to capture the nanoparticles, but leads to collisions between the individual nanoparticles and the formation of larger aggregates. These larger aggregates have a much higher collective magnetization, due to the increased volume, and this increases their motion, and thus the probability of further collisions[133]. This cascade effect results in the separation and capture of long nanochains in solutions, and have also been performed in the gas phase[46–48,52,134]. Magnetic nanoparticles can therefore only be separated and captured using an applied magnetic field if the particle concentration in the gas, or solution, is sufficiently high.

The particles generated in this work are small, and the particle concentration in the gas is low ($<10^6$ particles cm^{-3}). Due to the low particle concentration in the gas, the magnetic aerosol nanoparticles do not collide and form nanochains in the gas flow. It is, therefore, not possible to capture the individual aerosol nanoparticles with a magnetic field alone while the nanoparticles are transported in the gas flow. Additional force acting on the nanoparticles is required. An ESP was used to ensure that the magnetic nanoparticles were captured and deposited with a controllable particle concentration profile and a predictable deposited particle concentration. Deposition in a combined electric and magnetic field was performed by placing a permanent magnet inside the ESP to generate an external magnetic field, allowing the magnetic interactions between magnetic aerosol nanoparticles close to the substrate to be studied.

Nanoparticle deposition in an MESP

The deposition and assembly of differently magnetic (ferro- and diamagnetic) 50 nm nanoparticles, with and without an applied magnetic field, is shown in Figure 4.3. The diamagnetic Au nanoparticles assemble as weakly interacting nanoparticles[41,135], with most nanoparticles in direct contact with the substrate, and a few nanoparticles deposited on top of the already deposited nanoparticles. The addition of a strong magnetic field did not influence the assembly of these nanoparticles (Figure 4.3a-c). In contrast, the ferromagnetic Ni nanoparticles assembled into larger, elongated clusters that extended in various directions (Figure 4.3d). Applying a magnetic field during deposition of Ni nanoparticles changed the assembled structure considerably. Instead of forming clusters extended in various directions, the nanoparticles assembled into aligned nanochains which, when imaged from the side, appeared to be growing vertically out of the substrate plane (Figure 4.3e-f).

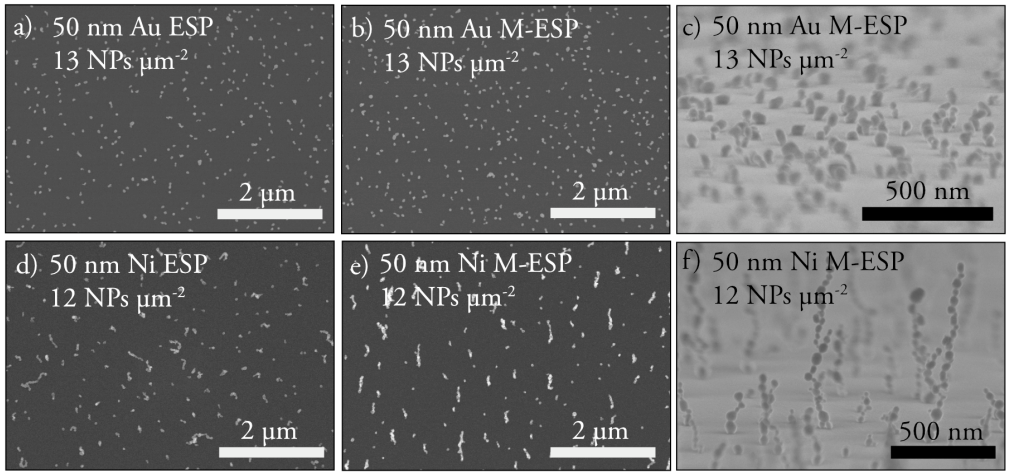

Figure 4.3. Comparison of diamagnetic Au and ferromagnetic Ni nanoparticle deposition in an ESP and an MESP with similar deposited nanoparticle (NP) concentration. The Au nanoparticles were not affected by the external magnetic field, and the clusters are characteristic of weakly interacting nanoparticles (a-c). The Ni nanoparticles, on the other hand, assembled differently (d-f). Without the external magnetic field, they showed a high tendency to form clusters of branched structures extending in various directions (d). When an external magnetic field was applied out of the plane, the nanoparticles assembled into straight vertically oriented nanochains (e-f). The SEM images in *a*, *b*, *d*, and *e* were acquired at a 30° tilting angle, and the SEM images in *c* and *f* were acquired from a side view.

The self-assembly of magnetic nanoparticles was further studied with other ferromagnetic elements (Fe and Co), as well as differently sized Co nanoparticles (20, 30, 40, and 50 nm). Significant chain formation was observed for all the ferromagnetic nanoparticles, as can be seen in Figure 4.4. The magnetization of the ferromagnetic dipole is equal to the product of the saturation magnetization and the volume of the dipole. Large nanoparticles with high saturation magnetization are therefore expected to show a high tendency to self-assemble. Ni, with the lowest saturation magnetization of the materials studied (see Table 4.1), formed short, densely packed nanochains, whereas Co self-assembled into long, widely separated nanochains. Fe has the highest saturation magnetization of the materials studied, however, this is not reflected in its deposition. Fe formed long nanochains, similar to Co, but a large fraction of Fe nanoparticles was also deposited directly onto the substrate, similar to the case in Au deposition. This suggests that some of the Fe nanoparticles are strongly interacting, while others are weakly interacting.

The deposition of differently sized Co nanoparticles revealed that self-assembly into nanochains could be achieved in this entire size range (Figure 4.4e-h). The larger nanoparticles have a much larger volume, and thus a higher magnetization. The distance at which an already deposited nanoparticle can effectively attract and capture a nanoparticle in the gas is much greater for the larger nanoparticles than for smaller ones.

Consequently, the deposited particle concentration required to observe significant nanochain formation will be much lower for larger nanoparticles than for smaller ones.

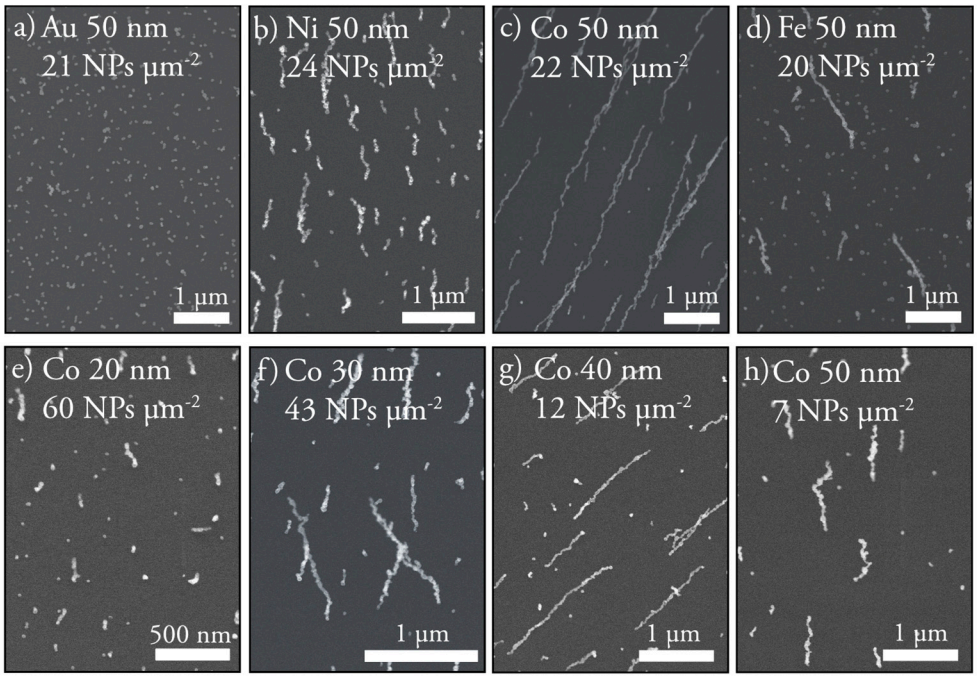

Figure 4.4. Nanochain formation of different materials (Au, Ni, Co, and Fe) (a-d) and differently sized Co nanoparticles (20, 30, 40, and 50 nm) (e-h) at different deposited nanoparticle (NP) concentrations. Ni, Co, and Fe self-assembled into chain-like structures, Co formed long nanochains, whereas Ni self-assembled into shorter, denser nanochains (b-d). The deposition of Fe was differed from that of Co and Ni (d). Some nanoparticles assembled into long nanochains, similar to Co, while others were deposited similarly to the weakly interacting Au nanoparticles. The deposition of differently sized Co nanoparticles revealed nanochain formation over the size range from 20 to 50 nm (e-h). A lower deposited particle concentration is needed to form long nanochains of larger nanoparticles.

Quantification of self-assembly

A measure was constructed to compare and quantify the self-assembly and deposition of different nanoparticles. The *fraction of particles on the substrate* can be obtained by dividing the number of nanoparticles deposited in direct contact with the substrate (per unit area) by the total number of nanoparticles deposited (per unit area). For weakly interacting nanoparticles, almost all nanoparticles initially end up in direct contact with the substrate, and a large number of nanoparticles is needed before substantial cluster formation occurs. The fraction of particles on the substrate is then initially close to 1, and decreases slowly. For strongly interacting nanoparticles, most nanoparticles assemble on top of an already deposited nanoparticle, and not in direct contact with the substrate, and the fraction of particles on the substrate decreases rapidly.

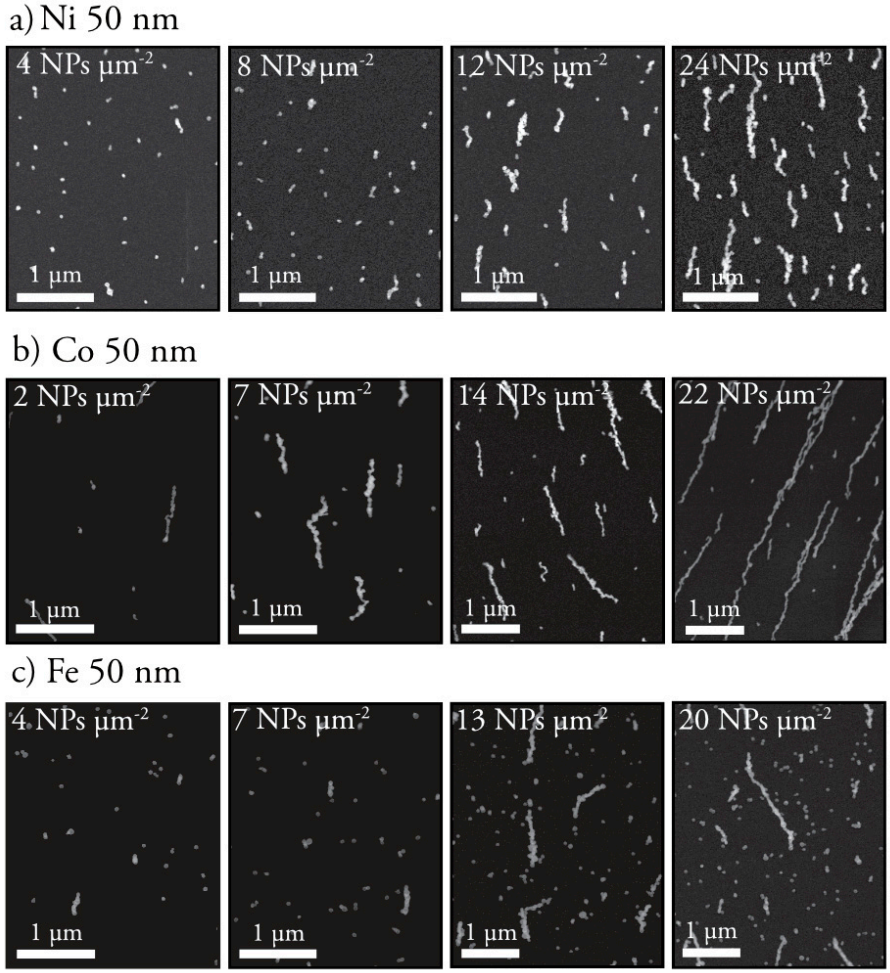

Figure 4.5. The evolution of self-assembled nanostructures. Ni and Co formed long separated nanochains with only a few single nanoparticles deposited onto the substrate (a-b). The Co nanochains grow rapidly and long nanochains can be seen at low deposited particle concentration. In the case of Fe, a larger number of deposited nanoparticles do not contribute to nanochain formation (c). These nanoparticles are deposited closed to each other, as weakly interacting nanoparticles.

To determine the fraction of particles on the substrate experimentally, and to visualize the trends with increasing deposited particle concentration, several experiments were performed with different deposited particle concentrations. The deposited particle concentration on the substrate is calculated using Equation 3.10 in Chapter 3 (*Paper II*). The number of particles deposited in direct contact with the substrate was calculated from multiple SEM images for each deposition. Each imaged cluster in the SEM image is assumed to be composed of one nanoparticle in direct contact with the substrate, and the rest of the deposited nanoparticles are assumed to be located in the cluster. For low

deposited particle concentrations, when the length of the nanochains is still small, it is simple to estimate the number of deposited particles in direct contact with the substrate (see leftmost column in Figure 4.5). However, as the nanochains grow longer the probability of two nanochains interacting and merging increases (see rightmost column in Figure 4.5). These images are more difficult to analyze, and for high deposited nanoparticle concentration the length and interactions between the nanochains makes the SEM images almost impossible to interpret.

The results from the deposition experiments are plotted as data points in Figure 4.6, showing the expected rapid decay of large Co nanoparticles. Ni and Fe follow similar trends, whereas for Au, a large fraction of the nanoparticles is in direct contact with the substrate, even at high particle concentrations. These results are compared to numerical simulations (solid lines in Figure 4.6), and the model used for the simulations is presented in the next section.

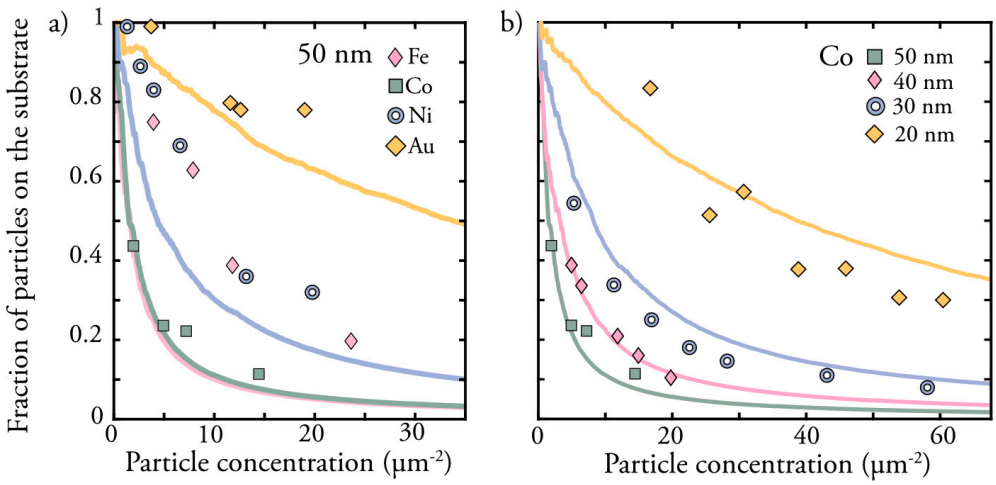

Figure 4.6. Experimental data points and simulations (solid lines) of the deposition of different nanoparticles. Co, with high saturation magnetization, and the larger nanoparticles show a strong tendency to self-assemble. A small number of nanoparticles are needed before most of the deposited particles form a cluster. For weakly interacting Au nanoparticles and smaller Co nanoparticles, a much higher number of deposited nanoparticles are needed to reaching this point.

Simulations of aerosol nanoparticle deposition in an MESP

Many numerical simulations of the deposition of aerosol nanoparticles, with and without electric fields, have been reported[41,136–139]. However, the magnetic interactions between magnetic nanoparticles have not been studied previously. The model used in this work to simulate the deposition of magnetic nanoparticles is based on an earlier study on charged nanoparticle deposition in an electric field presented by Krinke et al.[41], adapted to include magnetic interactions. The nanoparticle trajectory is calculated by determining the

change in particle momentum using Newtonian mechanics, which is the same approach as that used in the COMSOL Multiphysics simulations described in Chapter 3. However, other forces are more dominant and relevant for the simulations described here. For example, the gas velocity is set to zero, and Brownian motion and interparticle interactions dominate the nanoparticle trajectory (see simulated trajectories in Figure 4.7).

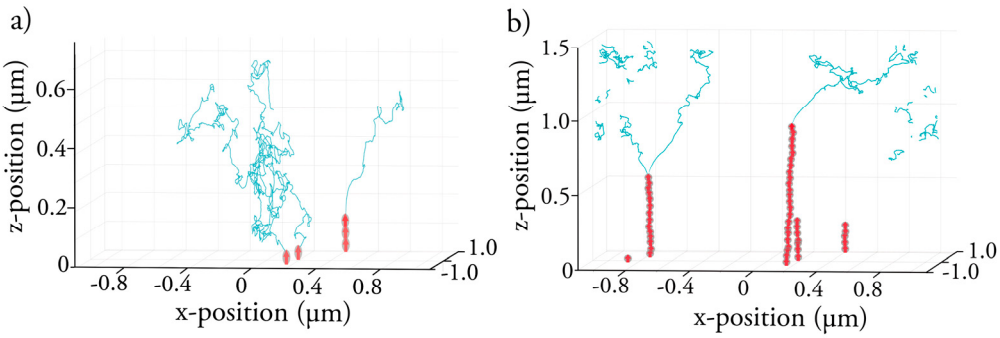

Figure 4.7. Simulated trajectories of 50 nm Co nanoparticles. Initially, when no, or only a few, nanoparticles have been deposited, the trajectory of nanoparticles in the gas is mainly governed by Brownian motion and the constant electric force attracting them towards the surface (a). After several nanoparticles have been deposited the trajectories start to differ. Far from the substrate, the trajectories are still governed by Brownian motion, but at long distances, the nanoparticles in the gas also become strongly attracted by the already deposited nanoparticles, leading to nanoparticles in the gas being deposited on top of already deposited nanoparticles (b).

To calculate the magnetic force (F_{M}), the nanoparticles are regarded as magnetic dipoles with a magnetization $M = M_{\mathrm{S}}V$ where M_{S} is the saturation magnetization and V is the volume of the nanoparticle. The magnetization is initially set to a random direction for the incoming nanoparticle, and is aligned with the local magnetic field in each time step, calculated from the previous iteration. The magnetization of the first released nanoparticle deposited with an out-of-plane magnetic field instantly aligns with the external magnetic field. Instantly alignment of the magnetization is based on the assumption that any possible magnetic anisotropy can be neglected, and that the nanoparticles can rotate freely in the gas without considering torque.

The total magnetic force acting on the nanoparticle in the gas is approximated by the contribution from the external magnetic field (H_{ext}) and the contribution from all the already deposited nanoparticles, and is given by the following equation,

$$F_{\mathrm{M}} = \mu_0 \int \nabla(M_{\mathrm{S}} \cdot H_{\mathrm{ext}})\, dV + \sum_i F_{\mathrm{Di,M}}(r, i). \tag{4.1}$$

where $F_{\mathrm{Di,M}}$ is the force between two magnetic dipoles, derived by Yung et al.[140]. In the present simulations the external magnetic field was assumed to be homogeneous on this length scale, hence $\nabla H_{\mathrm{ext}} = 0$. The total magnetic force acting on a particle in the gas at a position r is therefore equal to the total dipole – dipole force contributions from all the already deposited nanoparticles with index *i*.

$$F_{\mathrm{M}} = \sum_{i} F_{\mathrm{Di,M}}(r, i) \tag{4.2}$$

Further information on the simulations can be found in Supplementary Material to *Paper III*.

Significance of the magnetic force in an MESP

The simulations of the deposition and self-assembly of ferromagnetic nanoparticles revealed that the effect of the magnetic force is highly significant. The magnetic force influenced especially large Fe and Co nanoparticles, as can be seen in Figure 4.8. The magnetic force was less important for smaller nanoparticles and had an almost insignificant effect on the 10 nm Ni particles (Figure 4.8a).

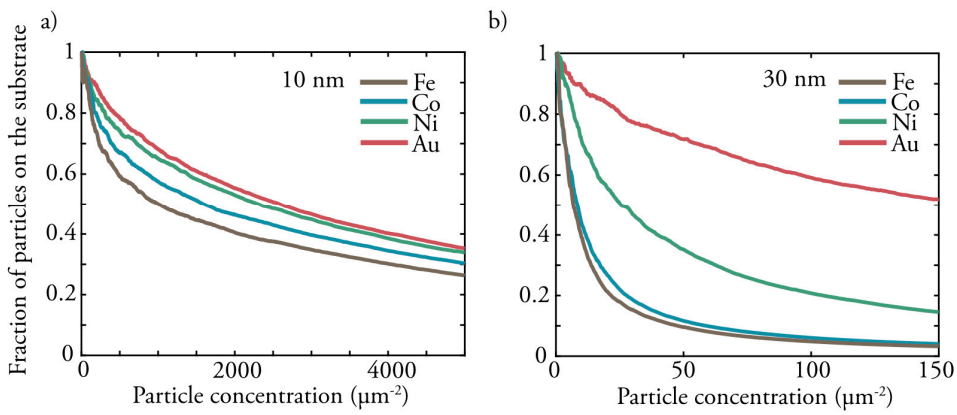

Figure 4.8. The importance of including the interactions with the magnetic force in the simulations is visualized by comparing the simulations for Au nanoparticles with those for the ferromagnetic nanoparticles. For large nanoparticles with a high saturation magnetization the fraction of particles on the substrate decreases rapidly. The differences between the ferromagnetic and diamagnetic nanoparticles are not as significant for small nanoparticles, and a large number of particles is needed before the difference is observed.

The strength of the magnetic force in relation to all the other forces included was measured by forcing a Co nanoparticle closer towards an already deposited Co nanoparticle, step-wise. The total force, together with the magnetic force contribution, is

plotted for different nanoparticle sizes in Figure 4.9a. It can be seen that the magnetic force is, in principle, the only contribution to the total force in this size range, and that the magnetic force becomes dominant at longer particle distances for the larger nanoparticles. Only for small 10 nm nanoparticles separated by a small distance does the magnetic force have a minor influence. As deposition and self-assembly proceed, nanochains are formed, and the effect of adding several nanoparticles on top of each other was also calculated (Figure 4.9b). The already strong interparticle attraction was amplified when several nanoparticles were stacked on top of each other. Large nanochains are therefore more likely to attract nanoparticles in the gas for further growth.

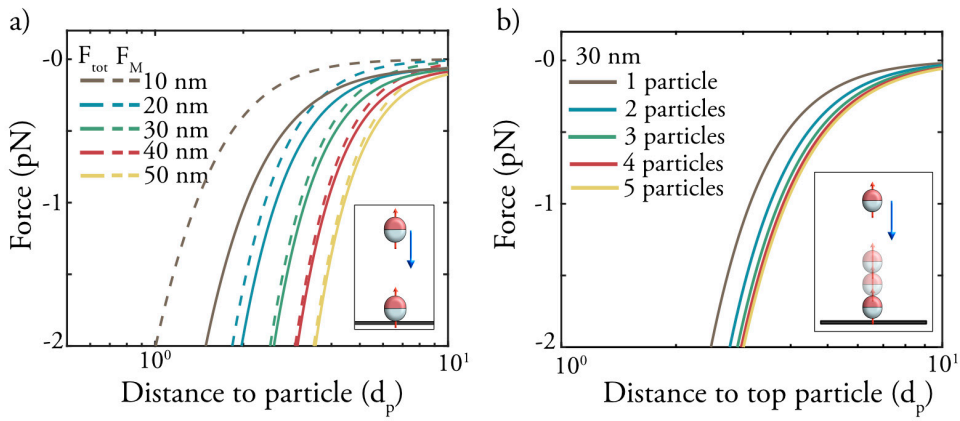

Figure 4.9. The total force and the contribution of the magnetic force on a nanoparticle that is moved step-wise closer to an already deposited nanoparticle (a). In the size range 20-50 nm, the magnetic force is in principle the only contribution to the total force. Adding several nanoparticles on top of each other amplifies the magnetic force and the tendency for further growth (b).

Directed self-assembly of nanoparticles

The magnetic aerosol nanoparticles experience a strong interparticle attraction, forcing nanoparticles in the gas to be deposited onto the already deposited nanoparticles, as illustrated by both the deposition experiments and simulations. This enables the formation of bottom-up vertically grown self-assembled nanostructures using individual nanoparticles as building blocks. The results presented so far were obtained with a 0.47 T out-of-plane magnetic field. In this section, the effect of the strength and direction of the applied external magnetic field, and the effects on self-assembly, are further discussed.

External magnetic field strength and orientation

Co nanoparticles deposited with applied magnetic field strengths of 0.47, 0.09, and 0 T showed a similar tendency to self-assemble, as can be seen in Figure 4.10a. Simulated deposition of magnetized Co nanoparticles revealed the same trends. These results suggest that the Co nanoparticles are spontaneously magnetized in the gas, and that the applied magnetic field does not have a significant influence on their tendency to self-assemble. SEM images and simulations revealed that the applied magnetic field instead influences the morphology of the nanochains by aligning the magnetization of the individual nanoparticles (Figure 4.10b-e). The magnetic nanoparticles self-assemble into straight, vertically growing nanochains when an out-of-plane external magnetic field was applied (Figure 4.9b-c). When no magnetic field was applied, the nanoparticles in the gas were still strongly attracted to the already deposited nanoparticles. However, without the external magnetic field, there is no preferable direction for the alignment of the nanoparticles. The growth of the nanochains becomes fractal-like, and the nanochains extend in different directions (Figure 4.10d-e).

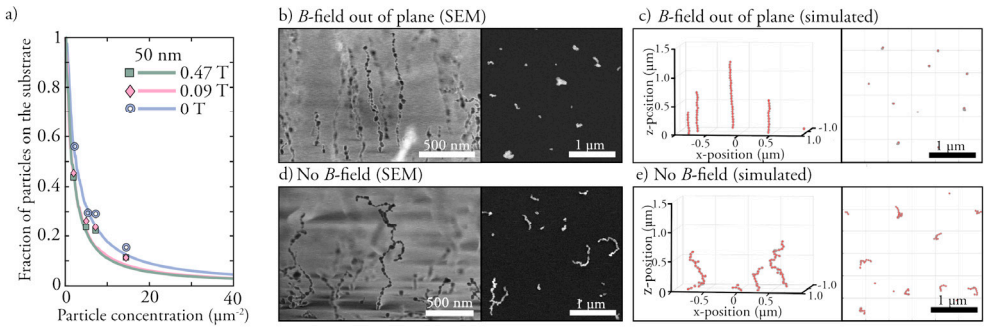

Figure 4.10 Experimental data and simulations revealed that the tendency to self-assemble was not significantly affected by the strength, or presence, of an external magnetic field (a). The main difference between deposition with, and deposition without, a magnetic field is the direction of alignment and growth of the chains. Nanoparticles deposited with an out-of-plane magnetic field form vertically aligned nanochains (b-c), whereas nanoparticles deposited without a magnetic field assembled into fractal-like structures (d-e).

The external magnetic field in the MESP facilitates self-assembly, and can be applied in various directions, to form differently aligned nanochains. For example, when the magnetic field is applied in-plane, nanochains are formed with an in-plane alignment (see Figure 4.11a). Deposition can also be performed with alternating magnetic field directions, and with different nanoparticle sizes. Figure 4.11b-d demonstrates three possible combinations. In *b* the deposition in *a* was continued after rotating the magnetic field 90° in the substrate plane. In *c* the combination in *b* was continued with two additional 90° rotations. Lastly, in *d*, a combination of differently sized nanoparticles and magnetic field directions was used. In this last combination, 40 nm Co nanoparticles were first deposited with an out-of-plane external magnetic field to form vertically growing

nanochains. This deposition was then continued by depositing 20 nm Co nanoparticles with an in-plane magnetic field. It can be seen in the SEM image that the 20 nm nanoparticles have a strong tendency to assemble on the already formed vertical nanochains, but growth continuous along the substrate plane to form T-shaped, branched nanostructures.

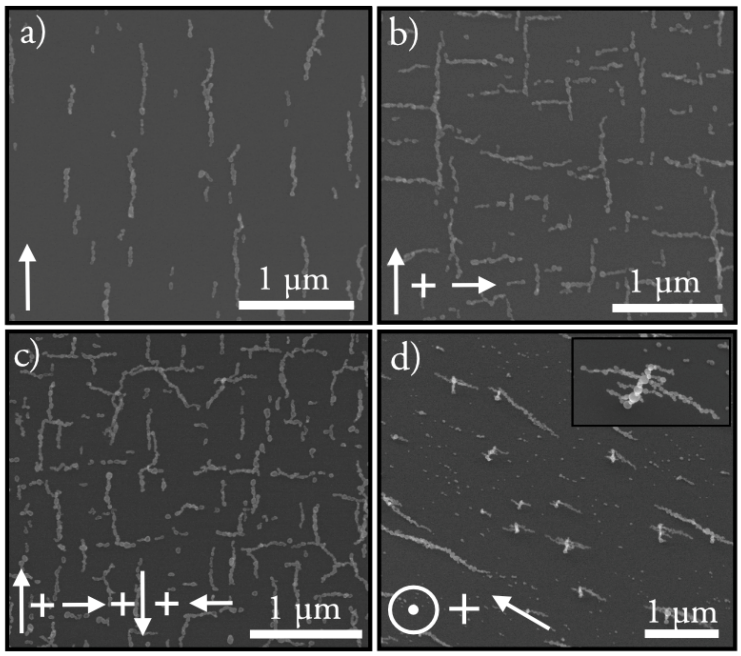

Figure 4.11 Magnetic-field-directed self-assembly can be performed in various directions and combined on the same substrate. In *a-c* an in-plane external magnetic field was used. In *a* the magnetic field was place in-plane, and then in *b* growth was continued after rotating the magnetic field 90°, while in *c* the magnetic field was rotated 90° three times. Such combinational depositions can also be performed with an out-of-plane and in-plane magnetic field, and with differently sized nanoparticles. In *d* 40 nm particles were first deposited with an out-of-plane magnetic field, and then 20 nm particles were deposited with an in-plane magnetic field to form branched nanostructures. The SEM images in *a-c* were acquired from a top view, while the SEM image in *d* was acquired at a 30° tilting angle.

Bundle formation and oriented macrostructures

The self-assembled nanostructures presented so far have all been generated with a relatively low deposited nanoparticle concentration. Each individual nanochain then grows independently, without significant influence from other nearby nanochains. When increasing the number of nanoparticles deposited, thus forming longer nanochains, it is likely that two or more nanochains will start to interact. Nanochains self-assembled with an out-of-plane magnetic field initially form vertically aligned nanostructures. As the chains start to interact and wiggle, bundles are formed and align in, what appears to be, random directions (see Figure 4.12a).

When an in-plane magnetic field was applied, the bundles were highly oriented, with nanochains aligned in the same direction, forming a large nanostructure with highly aligned and ordered magnetization (Figure 4.12b). More advanced structures can be assembled with more complex magnetic fields. Nanostructured patterns can be formed, with bundles aligned in different ways on the substrate, using a customized Polymagnet®, with magnetic north and south poles on the surface[141]. The bundles align in the same way as a macroscopic powder would (see Figure 4.12c-e). This indicates that it would be possible to form nanostructures with a tailored orientation on the substrate.

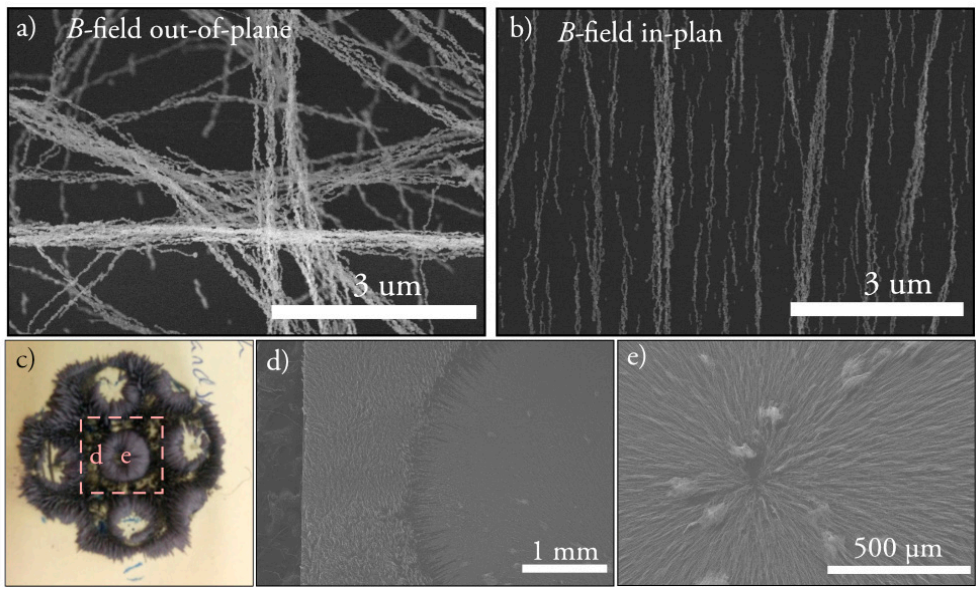

Figure 4.12. Nanochains form bundles that are aligned with the external magnetic field. When the magnetic field was applied out-of-plane, the nanochains first grow vertically out-of-plane. When the nanochains collapse into bundles, they arrange in different directions (a). When the magnetic field was applied in-plane, the nanochains and bundles tend to align in the same orientation as the magnetic field (b). A Polymagnet with a specialized magnetic surface generated the following pattern when a magnetic micropowder was placed on top of the magnet (c). The dash colored lines in *c* indicate where on the magnet the substrate was placed during aerosol nanoparticle deposition, and the letters d and e indicate where on the substrate the SEM images in *d* and *e* were acquired. A similar pattern to that seen with the micropowder was seen when depositing nanoparticles onto a substrate using the specialized Polymagnet (d-e). The particles in *d* and *e*, and the micropowder in *c* are aligned toward the center (c-e).

In this chapter a method to self-assemble magnetic nanoparticles into nanochains and bundle structures has been described. The possibilities of influencing the self-assembly by varying the magnetic field direction has also been demonstrated. The next chapter describes the creation of more complex multicomponent nanoparticles by mixing the magnetic material with another element with a specific property.

5. Multifunctional nanostructures

This chapter describes the creation of new types of nanostructures with tailored properties for specific applications, based on the developments described in the previous chapters. Two different materials were used to form multifunctional nanoparticles, one of which has high magnetization, while the other material is chosen based on the desired application. The nanoparticles preserve some of their magnetization and ability to self-assemble, as well as an additional property depending on the other element. The self-assembly of CoPd and CoAu nanoparticles and the catalytic activity of CoPd nanoparticles are described below as a proof of concept.

Generation and self-assembly of multifunctional nanoparticles

Multicomponent magnetic nanoparticles composed of two different materials were generated, and their self-assembly studied. Co, with high magnetization, was combined with Pd or Au to form CoPd and CoAu nanoparticles. A Co electrode was used as the anode, together with a Au rod or a Pd rod, and the compositions of the different types of nanoparticles are presented in Table 5.1.

Table 5.1. Composition of the nanoparticles generated. The data are based on XEDS measurements of individual nanoparticles using STEM. The standard deviation (SD) is based on 30-50 measured nanoparticles for each system.

Nanoparticle composition	Co (at. %)	SD (at. %)	Co (wt. %)
Co (anode) & Au (cathod)	73	3	45
Co (anode) & Pd (cathod)	57	3	42

As mentioned in Chapter 2, in nanoparticle generation by spark ablation, different materials lead to different ablated mass[59]. When using a pair of electrodes of two different materials, it is expected that more material will ablate from one of the electrodes than the other, influencing the nanoparticle composition. Apart from the material of the electrodes, the diameter of the rods, and whether or not the electrode is the cathode or anode also influences the mass ablated. Greater mass is ablated from a smaller diameter rod[71], and the electrode that initially acts as the cathode typically releases more material[65].

For the systems studied in this work, a Co electrode with a diameter of 5 mm was used as the anode, and a 3 mm diameter Au rod or a 5mm Pd rod was used as the other electrode. It has previously been shown that Au ablates more than twice as much as Pd, when generating AuPd nanoparticles[70]. Based on this, it is expected that the Au electrode should ablate more than the Pd electrode, and that the multicomponent nanoparticles would contain more Au than Pd. However, the weight percent (wt. %) of Pd and Au in the nanoparticles formed was almost identical (Pd 58 wt. % and Au 55 wt. %). Few studies have compared the ablated mass from the electrodes in terms of the nanoparticle composition when using different electrodes. The findings presented here suggest that the final composition of the multicomponent nanoparticles is not directly related to the predicted ablated mass, and further studies are needed on this topic.

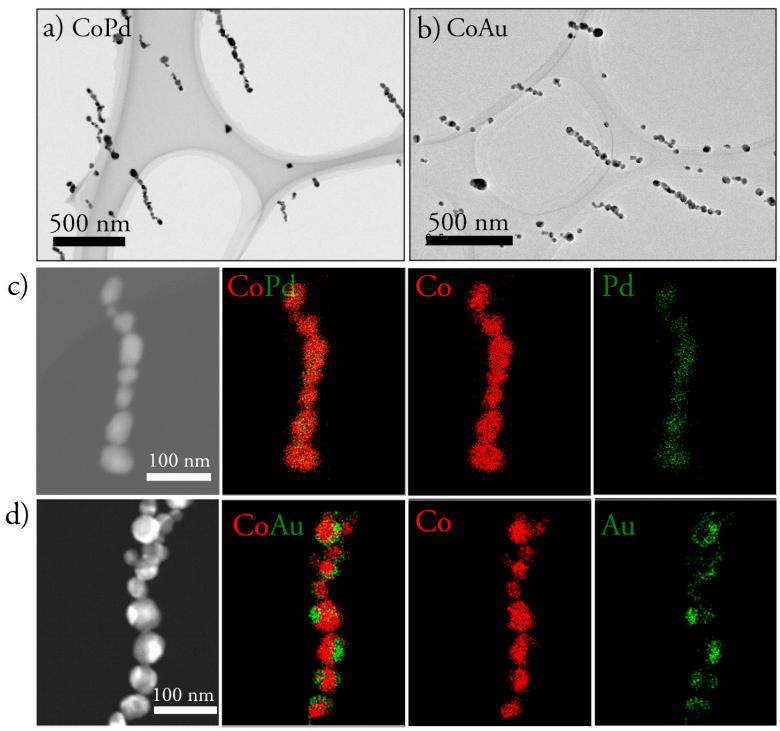

Figure 5.1. Self-assembled nanochains composed of CoPd (a) and CoAu (b). Based on XEDS mapping, the Co and Pd appeared to be uniformly distributed throughout the nanochain (c). The CoAu nanoparticles appeared to have separated into a Janus-type structure (d).

Both the CoPd nanoparticles and the CoAu nanoparticles self-assembled into nanochains when deposited in the presence of a magnetic field (see Figure 5.1a-b). By investigating the composition of the individual nanoparticles, it was shown that the components in these CoPd and CoAu multicomponent nanoparticles were distributed differently. STEM

imaging and XEDS mapping revealed that Pd was uniformly distributed throughout the entire nanoparticle, whereas Au was separated from the Co (Figure 5.1c-d).

It is expected that mixing magnetic Co with another element would reduce the tendency to self-assemble, as fewer atoms in the nanoparticle would have an intrinsic magnetic atomic moment, and this leads to lower magnetization of the nanoparticles. Self-assembly of 40 nm CoPd nanoparticles was quantified and the results are compared to Co, Pd and CoPd in Figure 5.2a. The saturation magnetization of the CoPd nanoparticles in the simulations was assumed to be 57 % of that of pure Co, since the nanoparticles composed of 57 at. % Co. As expected, the tendency of the CoPd nanoparticles to self-assemble was lower than for the Co nanoparticles. However, it was significantly higher than for the Pd nanoparticles, and nanochain formation was observed (Figure 5.2b-d).

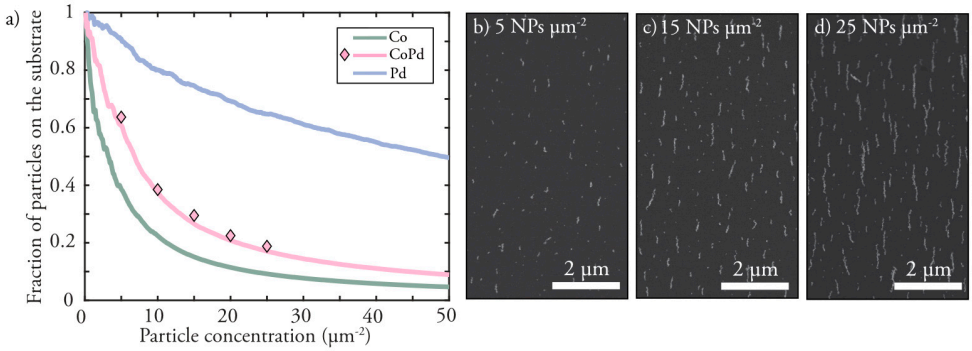

Figure 5.2. The self-assembly of CoPd nanoparticles was quantified and compared with those of Co and Pd (a). Despite that the CoPd nanoparticles contained only 57 at. % Co, self-assembly was very apparent. The saturation magnetization of the CoPd nanoparticles in the simulations was assumed to be 57 % of that of pure Co. Self-assembly of the CoPd nanochains generated with different deposited nanoparticle (NP) concentration was very similar to the ferromagnetic materials shown in Chapter 4 (b-d).

Heterogeneous catalysis and CO oxidation

Catalysis is a surface-related phenomenon. Surface atoms of the catalytic material experience a different environment from atoms in the bulk, which usually makes them more reactive. In heterogeneous catalysis the reactants and catalyst are in different phases, for example, solid catalytic nanoparticles reacting with gas molecules. The catalytic material assists by providing an energetically favorable pathway for the reaction, by lowering the energy barrier, which allows the reaction to proceed faster, or at lower temperatures. It is vital that the catalyst assisting the gas reaction is not consumed.

Many catalytic materials are rare and expensive, and it can therefore be advantageous to mix the catalytic material with a cheaper element to reduce the cost. The mixing of

different components can also improve the catalyst. For example, nanoparticles with a noble metal – metal oxide junction have been shown to have enhanced catalytic activity[33,142].

CO oxidation

CO oxidation is one of the most studied reactions in the field of catalysis. The reaction is simple, as few, relatively small, components are involved. CO is a toxic gas that is formed during incomplete combustion, and catalytic oxidation is an effective way of removing CO and transforming it into the much less toxic CO_2. The oxidation of CO can be expressed in the following simplified reaction

$$2CO + O_2 -> 2CO_2.$$

This simple reaction pathway has made CO oxidation ideal for fundamental studies. Pd is a commonly used catalyst for this reaction due to its ideal reactivity that generates a high activity[143]. The activity of the Pd catalyst depends on factors such as, surface structure, particle size, and support[144].

Catalytic activity

As discussed in Chapter 4, self-assembled nanochains rapidly form a porous structure, which may extend over a large volume. Self-assembled nanochains have a high density of active sites that can allow for fast diffusion of the reactants, which might enhance the catalytic activity. Similar structures with a high surface area have shown potential in water-splitting catalysis[46]. CO oxidation of CoPd nanochains was studied to establish whether they were catalytically active.

Self-assembled nanochains consisting of 40 nm CoPd nanoparticles were synthesized with an in-plane magnetic field and the catalytic activity was measured and compared with that of deposited 40 nm Pd nanoparticles. The catalytic activity was investigated by measuring the CO_2 signal with planar laser-induced fluorescence (PLIF) just above the substrate as the temperature was increased (technical details can be found in Appendix). A high CO_2 signal was detected above both samples at similar temperatures indicating that both the Pd sample and the CoPd sample were catalytically active (Figure 5.3). These results indicate that the CoPd nanochains are multifunctional and demonstrate the possibility of forming catalytically active nanochains by allowing multicomponent aerosol nanoparticles to self-assemble in a combined electric and magnetic field.

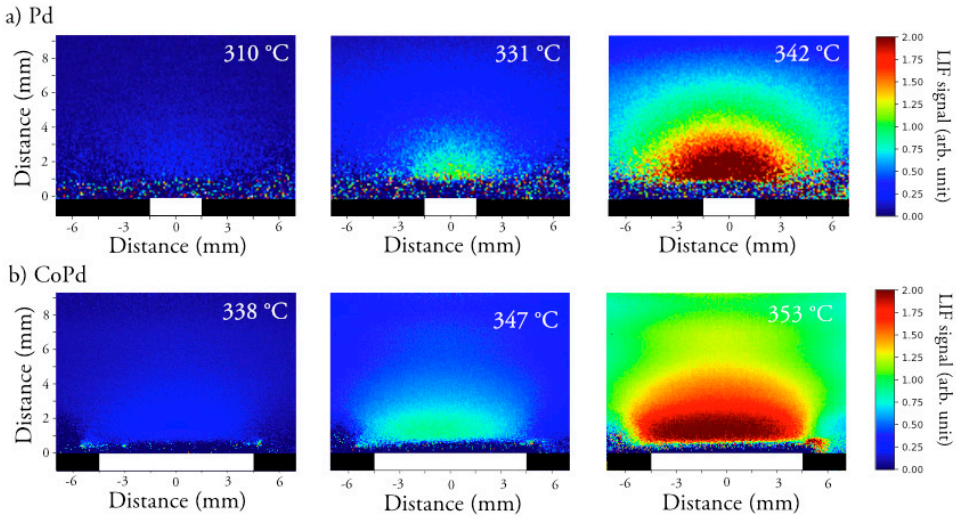

Figure 5.3. PLIF measurements of Pd and CoPd nanoparticles. The white boxes indicate the size and location of the samples. The two samples were catalytically active as a high CO_2 signal was detected above both samples at similar temperatures.

Nanoparticle and nanostructure stability

During the PLIF measurements, the samples were heated to roughly 400 °C and cooled several times. It is important that the catalyst does not undergo significant changes during the reaction to ensure reproducible performance and stability of the catalytic material. The CoPd and Pd nanoparticles were therefore investigated before and after the catalytic measurements. The self-assembled CoPd nanoparticles retained their chain structure, and remained highly ordered even after heating (Figure 5.4a-b). Some minor sintering was observed in the neck region of the nanoparticles, leading to slight changes in the morphology and size of the individual nanoparticles (Figure 5.4b). In contrast, the Pd nanoparticles assembled as weakly interacting nanoparticles, and formed small compact clusters on the substrate (Figure 5.4c). After heating and measuring the catalytic activity, these clusters appeared to be sintered together (Figure 5.4d).

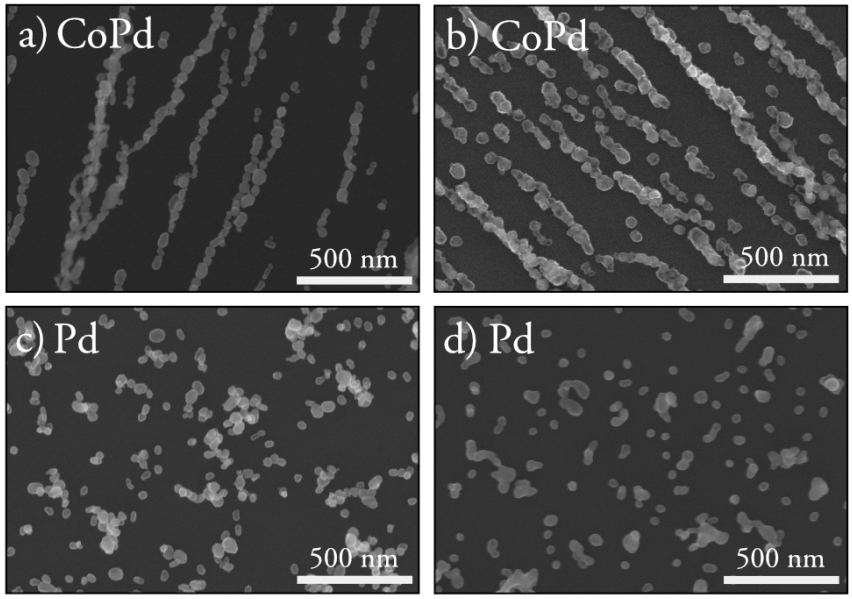

Figure 5.4. SEM images of CoPd (a-b) and Pd (c-d) nanoparticles before and after heating. The CoPd nanoparticles assembled into nanochains, whereas the Pd nanoparticles were deposited directly onto the substrate or in small dense clusters (a,c). After heating, both the CoPd nanochains and the Pd nanoparticles appeared to have sintered (b,d).

The observed sintering of the CoPd and Pd nanoparticles is undesirable, as it reduces the surface area, and thus the available surface atoms. The Pd clusters were more compact than the CoPd chains, and denser aggregates with fewer nanoparticles sinter more rapidly than elongated nanostructures[145,146]. According to molecular dynamics simulations by Hawa and Zachariah, the sintering time of a nanochain increases with the number of nanoparticles in the chain. Sintering occurs in a few steps. The chain is first transformed into a rod-like structure, followed by slow contraction of the rod[147]. At sufficiently high temperatures, the long nanochains are also expected to fragment[148,149]. It is difficult to know whether this has occurred or not in the case of CoPd nanoparticles based on the SEM images shown in Figure 5.4, and further studies are required on the stability of nanochains.

6. Conclusions

The studies described in this dissertation concerns the generation and assembly of aerosol nanoparticles in a controlled way to form nanostructures with desired properties. In this chapter, the main conclusions and what I believe are the main contributions of these studies are discussed first. Following this, a short outlook and some suggestions for future studies are given.

Main conclusions

Aerosol nanoparticle generation

The results presented here demonstrate the great potential of spark ablation for the production of both single-component nanoparticles and mixing different materials for the production of multicomponent nanoparticles. The former enabled the fast and simple study of nanoparticle deposition in an ESP, and the self-assembly of magnetic nanoparticles with different degrees of magnetization.

Multicomponent nanoparticles were generated using alloyed electrodes, and opposing electrodes of different materials. The FeCr and FeMn nanoparticles generated with alloyed electrodes had almost identical elemental ratios to those of the electrodes. However, it was difficult to predict the composition of the CoPd and CoAu nanoparticles, generated with two different opposing electrodes. Alloyed electrodes are therefore preferable to obtain predictable and desired nanoparticle compositions. The formation of multicomponent nanoparticles may also be limited by the vapor pressure of one of the components. If the temperature required for compaction is higher than that of the onset of evaporation for one of the components, it may be difficult to form the desired mixture.

I also continued the work performed by Hallberg et al.[89], who studied oxidation of single-component nanoparticles in a hydrogen-containing carrier gas, although I studied multicomponent nanoparticles with elements that are prone to oxidize. I showed that the shape of the nanoparticles in systems containing Fe could be altered between a self-passivated and a completely oxidized structure, depending on the carrier gas composition.

Aerosol deposition in an electrostatic precipitator

All the nanoparticles generated in this work were deposited with an ESP. COMSOL Multiphysics was used to model the nanoparticle deposition in an ESP, and the results were compared to experimentally determined depositions. This enabled the formulation of an expression for the spot size, which can also be used to determine the deposited nanoparticle concentration. I showed that the spot size depends only on the gas flow rate and the drift velocity of the nanoparticles in the electric field. I also showed that the deposited particle concentration is independent of the gas flow rate.

The total number of deposited nanoparticles could easily be predicted by monitoring the size distribution and particle gas concentration of the charged nanoparticles with a DMA in combination with an electrometer. This is a considerable advantage in ESP deposition. However, this advantage becomes impractical if the deposition profile and the nanoparticle concentration on the substrate are unknown. The formula derived is therefore extremely useful for predicting the deposited particle concentration on the substrate.

The formula has already been useful in my own research. For example, it would not have been possible to quantify the self-assembly as described in *Paper III* without being able to predict the deposited nanoparticle concentration. This formula can also be used to estimate the nanoparticle mass deposited on the substrate, which can be very useful for studies of the intrinsic properties of nanoparticles. I believe that these results, in particular the equation derived, are highly relevant for any application in which nanoparticles are sampled with an ESP. The equation could also be included in specification sheets for commercially available ESPs, or even in aerosol text books on aerosol sampling.

Multifunctional nanostructures enabled by self-assembly

COMSOL Multiphysics was used to determine the deposition of aerosol nanoparticles in an ESP from a macroscopical point of view. It does not calculate the trajectory of individual nanoparticles as they are less than 1 μm from the substrate. Close to the substrate, the interparticle interactions become more important, and the nanoparticles assemble into differently shaped structures depending on the intrinsic properties of the nanoparticles. The magnetic dipole – dipole interaction is strong, and enables the self-assembly of magnetic nanoparticles into nanochains.

I demonstrated a simple pathway for generating highly ordered nanostructures directly on a substrate by depositing magnetic nanoparticles in an MESP. The prerequisites are that the magnetic nanoparticles are aerosolized and charged upon deposition. I showed that self-assembled nanostructures can be generated by combining an electric and a magnetic field during deposition. The electric field in the ESP is necessary to force the

nanoparticles towards the substrate. The applied magnetic field aligns the magnetization of the magnetic nanoparticles, and directs nanochain formation and self-assembly on the substrate. Differently sized nanoparticles with varying composition were self-assembled into various nanostructures, by controlling nanoparticle generation and the magnetic field orientation.

The generation of nanoparticles by spark ablation enables mixing of a magnetic material with another material of choice, to assemble nanochains with desired properties. As a proof of concept, I demonstrated the possibility of forming multifunctional catalytically active CoPd nanostructures for CO oxidation. This demonstrates the potential of forming other multifunctional nanostructures with tailored compositions, and with specific properties.

Outlook

I have described how the self-assembly of magnetic aerosol nanoparticles into nanochains can be achieved and controlled, even when the magnetic material is combined with another material. This can be further studied by producing nanoparticles of different compositions and elemental ratios in order to study the effect on self-assembly of different amounts of the non-magnetic material in the nanoparticles. Nanoparticles composed of different material combinations can then be tailored based on the desired application.

Self-assembly of multicomponent nanoparticles was achieved with an MESP, and it would be interesting to perform fundamental magnetic studies on the nanochains and the magnetic exchange interactions. Other magnetic materials can also be studied, for example, Gd nanoparticles which have high saturation magnetization and zero remanent magnetization at room temperature. Such nanoparticles are ideal for studying the magnetocaloric effect, and it would be interesting to investigate how chain formation and possible alloy formation would influence this effect. Also, self-assembly was only studied on flat surfaces with a homogeneous magnetic field, and it would be interesting to study self-assembly on more complex substrates, for example, a micro-array or a grid, and with a varying magnetic field.

There are many interesting opportunities for further studies on self-assembled nanostructures enabled by aerosol nanoparticle deposition in an MESP. Hopefully, the findings presented will be valuable in future research, and inspire others to develop new materials for new applications. I hope I have provided some valuable insight for both the aerosol and the nanoscience community.

Appendix

The main measurement techniques used to collect the data presented in this dissertation are described in more detail in this appendix, which is intended for those studying and characterizing nanoparticles.

Aerosol instruments

Differential mobility analyzer

The DMA separates particles based on their electrical mobility. The principle behind the cylindrical DMA is relatively simple. The particles enter the DMA and are drawn through it by a high sheath gas flow. A high electrical potential is applied from a high-voltage source, exposing the particles in the sheath gas to a constant electrical force that is perpendicular to the drag force from the gas. Particles with opposite polarity to the high-voltage source are attracted, and depending on the applied potential, particles with different electrical mobility can be selected. Smaller particles with higher electrical mobility are collected on the high-voltage source, whereas larger particles with a lower electrical mobility, together with neutral particles, exit with the sheath gas (see schematic in Figure A.1).

The fact that the particles are selected based on their electrical mobility, and not their geometric size can cause problems, as larger particles that are doubly or multiply charged have the same electrical mobility as smaller singly charged particle, and will also be selected. Another problem associated with DMAs is that a large number of particles are lost, as all the neutral and positively charged particles are not selected.

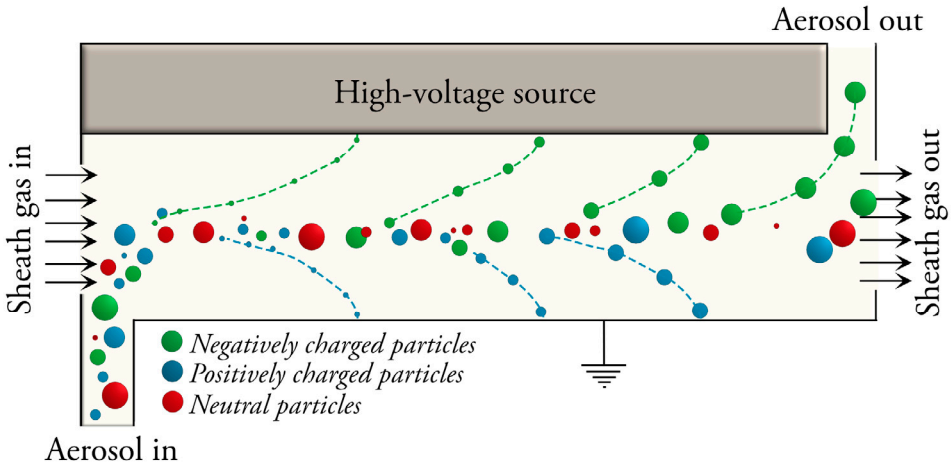

Figure A.1. Polydisperse particles enter the DMA, and a high sheath gas flow carries them through the DMA. A high-voltage source generates an electric field, which attracts particles with opposite polarity than the high-voltage source. Depending on the applied potential, particles with different electrical mobility can be collected. Small particles with high electrical mobility are deposited early in the DMA, while larger particles with low electrical mobility follow the sheath gas and are removed.

Electrometer

There are various ways of measuring the concentration of particles in a gas. The condensation particle counter operates by condensing vapor onto the particles so they grow and become large enough to be detected with a laser. The number resolution is very good, and this is a useful technique for detecting a low particle concentration in the gas. If the particles have already been size-selected with a DMA, all particles will have the same polarity and the particle concentration can be determined based on the total number of charges using an electrometer. The charged particles are collected on a filter and the induced current is measured. The detected particles are assumed to be singly charged, and the particle concentration in the gas (C_{gas}) is determined using the following equation,

$$C_{\mathrm{gas}} = \frac{I}{e n_{\mathrm{p}} Q} \tag{A.1}$$

where I is the measured current, e is the elementary unit of charge, n_{p} is the number of charges per particle, and Q is the gas flow rate.

Electron microscopy

Conventional optical microscopy is usually limited to the study of objects of the same size as the wavelength of visible light. In order to study smaller structures it is beneficial to use various kinds of electron microscopy, where much shorter wavelengths can be used to probe the material.

Scanning electron microscopy

The scanning electron microscope is a useful instrument for off-line analysis of aerosol nanoparticles. It is relatively fast and simple, and the magnification sufficiently broad to image both individual nanoparticles and larger nanostructures. When the electron beam interacts with the material, electrons and x-rays are released from the substrate and detected.

To image material with SEM, back-scattered and secondary electrons are detected. Back-scattered electrons are deflected by the atoms in the material, and the number of detected electrons depends on the atomic number of the material. It is therefore possible to differentiate heavier material from lighter when detecting back-scattered electrons. Secondary electrons are the result of the excitation of loosely bond valence electrons in the material. This signal is insensitive to atomic number, but the probing depth is much smaller and provides better spatial resolution compared to the back-scattered electrons. Secondary electrons were mainly used to investigate the nanoparticles and nanostructures imaged in this work. For more information on SEM, the reader is referred to *Principles and Practice of Variable Pressure/Environmental Scanning Electron Microscopy (VP-ESEM),* by Debbie J. Stokes, and in particular Chapter 2[150].

Transmission electron microscopy

The transmission electron microscope is an advanced and important instrument for characterization of aerosol nanoparticles. Similar to the scanning electron microscope, electrons are used to image the sample, however, the electrons in a transmission electron microscope have a much higher energy. For a transmission electron microscope to function optimally, the number of scattering events each electron undergoes must be small, and the substrate must be thin enough to ensure that the electron beam is transmitted through the sample.

When operating a transmission electron microscope, it is important to be aware of the different contrasts that can be observed. In bright-field mode, the transmitted electrons are detected below the sample. A bright field indicates that most of the electrons have not

been scattered, and a darker field indicates more scattering events. If the material is "thick", or consists of heavier atoms, the electrons will scatter more. The image will then appear darker, due to **mass-thickness contrast**, as shown in Figure A.2a. Furthermore, if the sample has a crystal structure, the orientation of the crystal will affect the scattering events, and the image may appear darker or lighter depending on how the crystal is oriented. Two identical nanoparticles may therefore have different image contrast depending on how they are oriented in space, due to **diffraction contrast**, as shown in Figure A.2b. Finally, at high magnification, it is possible to observe rows of atoms using the **phase contrast**, and this is usually referred to as the atomic resolution (see Figure A.2c). It is possible to determine the lattice distances in the crystal using phase contrast.

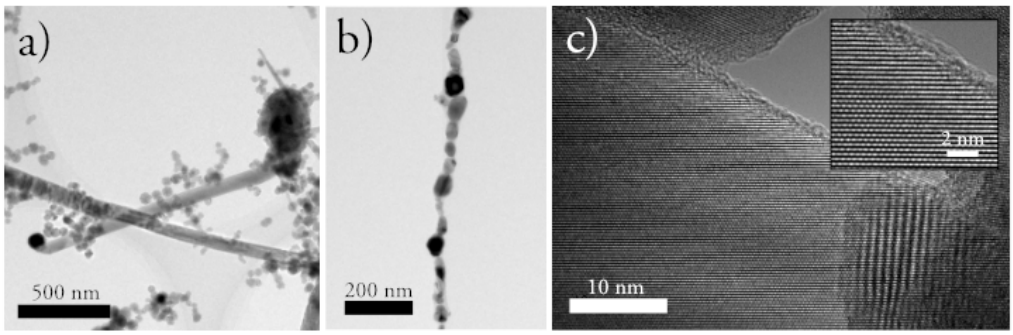

Figure A.2. TEM images showing three different types of contrast. Thicker or heavier regions will appear darker due to mass-thickness contrast (a), and the atoms in crystals in a specific orientation will appear darker due to diffraction contrast (b). Finally, rows of atom can be imaged using phase contrast (c).

The electron beam is not usually scanned in TEM, but instead focused to a small spot illuminating a small area. It is possible to operate the transmission electron microscope in scanning mode (STEM). In this work, STEM was used with a high-angle annular dark-field detector. Only scattered electrons are detected, and the background is therefore dark, (see Figure A.3). This imaging mode is particularly useful in achieving mass-thickness contrast, and eliminates diffraction contrast.

For further information on operation, and more details on TEM and STEM, the reader is referred to the comprehensive textbook, *Transmission Electron Microscopy: A Textbook for Materials Science* by Williams and Carter[151].

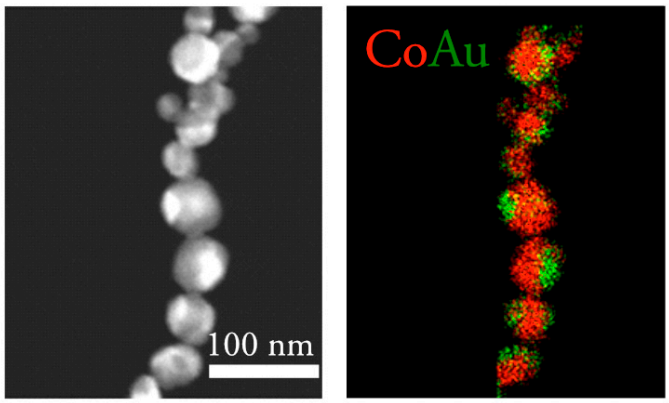

Figure A.3. Dark-field STEM image of CoAu nanoparticles acquired with a high-angle annular dark-field detector (left), together with the corresponding XEDS chemical mapping (right). The brighter areas in the STEM image are areas of nanoparticles containing heavier atoms. The image on the right reveals that the brighter areas correspond to the much heavier Au atoms and darker areas corresponds to Co atoms.

X-ray energy-dispersive spectrometry

XEDS is often used to determine the elemental composition of nanoparticles when operating an electron microscope, as it allows the composition of individual particles to be determined and mapped in great detail (see Figures A.3).

The electrons in the electron beam interact with the atoms in the sample and are scattered either elastically or inelastically. The energy lost during inelastic scattering may excite a core-level electron in the sample, creating an electron hole. When an electron from a higher energy state fills this hole, x-rays are released (see Figure A.4). The energy of the emitted x-ray is characteristic of the element. Although the x-ray signal is element-specific, it does not provide any information on the chemical state of the atom, for example, whether it is an oxide or a pure metal. This method is ideal for studying heavier metals, and the signal is difficult to interpret for lighter elements such as oxygen and carbon. For further details, the reader is referred to Part 4 in *Transmission Electron Microscopy: A Textbook for Materials Science* by Williams and Carter[151].

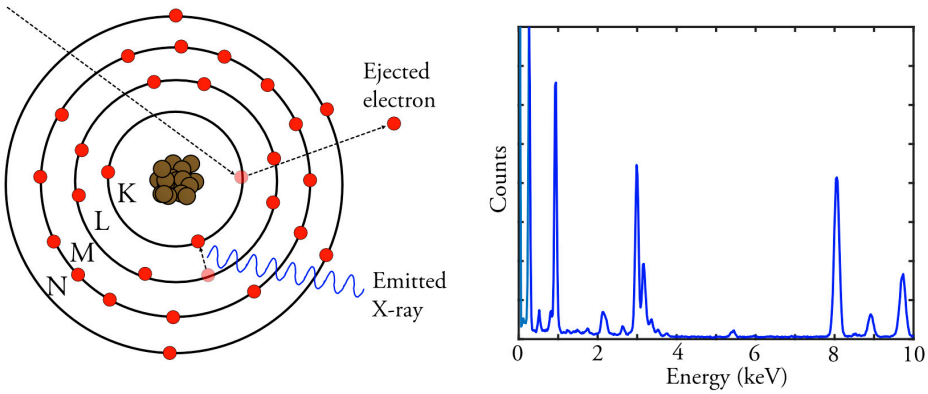

Figure A.4. An incoming electron scatters and ejects a core-level electron creating an electron hole. When an electron from a higher energy state fills this hole, characteristic x-ray is released (left). The energy of the emitted x-ray is detected and a spectrum with element characteristic peaks is generated (right).

X-ray photoelectron spectroscopy

XPS is a useful method for studying the surface composition of nanoparticles, and it provides information on the chemical state of the surface atoms. This method is ideal when studying core-shell nanoparticles or surface oxidation of nanoparticles. The principle of XPS is that a monochromatic x-ray beam is focused on the sample causing electrons to be ejected from the material (see Figure A.5). The kinetic energy of the ejected electrons is then detected and measured. Since the energy of the incoming photons is known, the characteristic binding energy of the measured electrons can be calculated.

Due to the short mean free path of the ejected electrons, only electrons ejected from the atoms located close to the surface are detected. All other electrons are scattered and absorbed in the material, making XPS a surface-sensitive technique. The energy of the ejected electrons provides information on the chemical state of the material, and it is possible to determine whether an oxide has formed on the surface or if it is a pure metal.

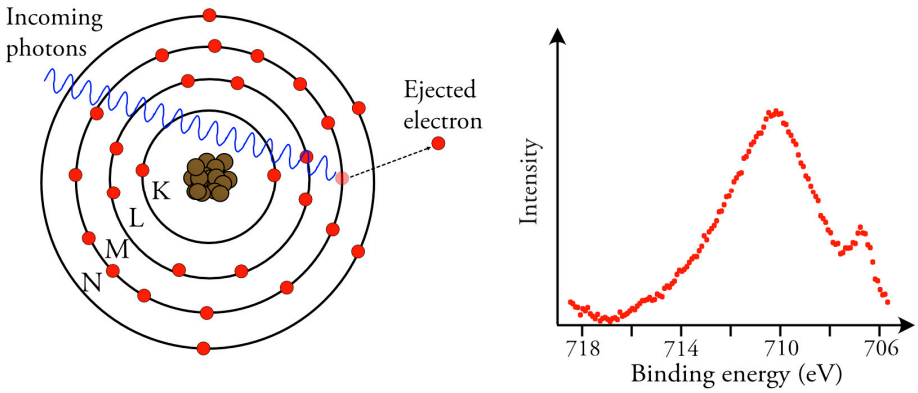

Figure A.5. Incoming photons ejects electrons from the atoms of the material (left). The energy of the ejected electrons is measured and provides information on the chemical state of the atoms located close to the surface (right).

Planar laser-induced fluorescence

The composition of a gas during a catalytic reaction is typically determined by mass spectrometry, but the signal contains no spatial information. Using planar laser-induced fluorescence (PLIF), it is possible to obtain a signal with spatial resolution over time. A 2D sheet of laser light at a wavelength that matches the energy level of the gas molecules to be probed is created. The laser sheet is sent through the reactor above the catalytic material, and the signal is detected with a camera. The laser excites the gas molecules, and when they relax fluorescence light is emitted, which is detected by the camera. A high absorption cross section can be obtained by tuning the wavelength of the laser to a specific energy transition of the gas molecules, which yields a high signal. Detection is therefore species specific, and it is possible to obtain spatial information on the gas concentration just above the surface of the catalytic material. For more information on PLIF measurements the reader is referred to Chapter 6 in the Springer Series in Chemical Physics Volume 114 *Operando Research in Heterogeneous Catalysis*[152].

References

1. Hinds, W. C. *Aerosol Technology: Properties, Behavior, and Measurement of Airborne Particles*. (John Wiley & Sons, INC, 1999).
2. Sorensen, C. M., Flagan, R. C., Baltensperger, U. & Pui, D. Y. H. Grand challenges for aerosol science and technology. *Aerosol Sci. Technol.* **53**, 731–734 (2019).
3. Kruis, F. E., Fissan, H. & Peled, A. Synthesis of nanoparticles in the gas phase for electronic, optical and magnetic applications—a review. *J. Aerosol Sci.* **29**, 511–535 (1998).
4. Biskos, G., Vons, V., Yurteri, C. U. & Schmidt-Ott, A. Generation and sizing of particles for aerosol-based nanotechnology. *KONA Powder Part. J.* **26**, 13–35 (2008).
5. Mäkelä, J. M. *et al.* Nanoparticle deposition from liquid flame spray onto moving roll-to-roll paperboard material. *Aerosol Sci. Technol.* **45**, 827–837 (2011).
6. Feng, J. *et al.* Scalable and Environmentally Benign Process for Smart Textile Nanofinishing. *ACS Appl. Mater. Interfaces* **8**, 14756–14765 (2016).
7. Sotiriou, G. A. & Pratsinis, S. E. Antibacterial activity of nanosilver ions and particles. *Environ. Sci. Technol.* **44**, 5649–5654 (2010).
8. Raliya, R., Saharan, V., Dimkpa, C. & Biswas, P. Nanofertilizer for Precision and Sustainable Agriculture: Current State and Future Perspectives. *J. Agric. Food Chem.* **66**, 6487–6503 (2018).
9. Magnusson, M. H. *et al.* Semiconductor nanostructures enabled by aerosol technology. *Front. Phys.* **9**, 398–418 (2014).
10. Heurlin, M. *et al.* Continuous gas-phase synthesis of nanowires with tunable properties. *Nature* **492**, 90–94 (2012).
11. Smail, F., Boies, A. & Windle, A. Direct spinning of CNT fibres: Past, present and future scale up. *Carbon N. Y.* **152**, 218–232 (2019).
12. Karlsson, M. N. A., Deppert, K., Magnusson, M. H., Karlsson, L. S. & Malm, J. O. Size- and composition-controlled Au-Ga aerosol nanoparticles. *Aerosol Sci. Technol.* **38**, 948–954 (2004).
13. Poostforooshan, J. *et al.* Aerosol process for the in situ coating of nanoparticles with a polymer shell. *Aerosol Sci. Technol.* **48**, 1111–1122 (2014).
14. Tabrizi, N. S., Xu, Q., Van Der Pers, N. M. & Schmidt-Ott, A. Generation of mixed metallic nanoparticles from immiscible metals by spark discharge. *J. Nanoparticle Res.* **12**, 247–259 (2010).

15. Yao, Y. *et al.* Carbothermal shock synthesis of high-entropy-alloy nanoparticles. *Science (80-.).* **359**, 1489–1494 (2018).

16. Yang, Y. *et al.* Aerosol Synthesis of High Entropy Alloy Nanoparticles. *Langmuir* (2020).

17. Feng, J. *et al.* Unconventional Alloys Confined in Nanoparticles: Building Blocks for New Matter. *Matter* 1–18 (2020).

18. Felser, C., Wollmann, L., Chadov, S., Fecher, G. H. & Parkin, S. S. P. Basics and prospectives of magnetic Heusler compounds. *Springer Ser. Mater. Sci.* **222**, 37–48 (2016).

19. Palmstrøm, C. J. Heusler compounds and spintronics. *Prog. Cryst. Growth Charact. Mater.* **62**, 371–397 (2016).

20. Wang, C. *et al.* Heusler nanoparticles for spintronics and ferromagnetic shape memory alloys. *J. Vac. Sci. Technol. B, Nanotechnol. Microelectron. Mater. Process. Meas. Phenom.* **32**, 020802 (2014).

21. Graf, T., Felser, C. & Parkin, S. S. P. Simple rules for the understanding of Heusler compounds. *Prog. Solid State Chem.* **39**, 1–50 (2011).

22. Ghosh Chaudhuri, R. & Paria, S. Core/shell nanoparticles: Classes, properties, synthesis mechanisms, characterization, and applications. *Chem. Rev.* **112**, 2373–2433 (2012).

23. Chen, Y., Yang, F., Dai, Y., Wang, W. & Chen, S. Ni@Pt core-shell nanoparticles: Synthesis, structural and electrochemical properties. *J. Phys. Chem. C* **112**, 1645–1649 (2008).

24. Pana, O. *et al.* Structure, morphology and magnetic properties of Fe–Au core-shell nanoparticles. *Surf. Sci.* **601**, 4352–4357 (2007).

25. Langlois, C. *et al.* Fully Crystalline Faceted Fe-Au Core-Shell Nanoparticles. *Nano Lett.* **15**, 5075–5080 (2015).

26. Zhang, J. *et al.* Laser-assisted synthesis of superparamagnetic Fe@Au core-shell nanoparticles. *J. Phys. Chem. B* **110**, 7122–7128 (2006).

27. López-Ortega, A., Estrader, M., Salazar-Alvarez, G., Roca, A. G. & Nogués, J. Applications of exchange coupled bi-magnetic hard/soft and soft/hard magnetic core/shell nanoparticles. *Phys. Rep.* **553**, 1–32 (2015).

28. Sangregorio, C. *et al.* Strongly Exchange Coupled Core|Shell Nanoparticles with High Magnetic Anisotropy: A Strategy toward Rare-Earth-Free Permanent Magnets. *Chem. Mater.* **28**, 4214–4222 (2016).

29. Binns, C. *et al.* Exchange Bias in Fe@Cr Core–Shell Nanoparticles. *Nano Lett.* **13**, 3334–3339 (2013).

30. Liu, F. *et al.* Building nanocomposite magnets by coating a hard magnetic core with a soft magnetic shell. *Angew. Chemie - Int. Ed.* **53**, 2176–2180 (2014).

31. Lattuada, M. & Hatton, T. A. Synthesis, properties and applications of Janus nanoparticles. *Nano Today* **6**, 286–308 (2011).

32. Xu, C. *et al.* Au-Fe3O4 dumbbell nanoparticles as dual-functional. *Angew. Chemie - Int. Ed.* **47**, 173–176 (2008).

33. Wang, C., Yin, H., Dai, S. & Sun, S. A general approach to noble metal-metal oxide dumbbell nanoparticles and their catalytic application for CO oxidation. *Chem. Mater.* **22**, 3277–3282 (2010).

34. Mahajan, A., Frisbie, C. D. & Francis, L. F. Optimization of aerosol jet printing for high-resolution, high-aspect ratio silver lines. *ACS Appl. Mater. Interfaces* **5**, 4856–4864 (2013).

35. Krinke, T. J., Fissan, H., Deppert, K., Magnusson, M. H. & Samuelson, L. Positioning of nanometer-sized particles on flat surfaces by direct deposition from the gas phase. *Appl. Phys. Lett.* **78**, 3708–3710 (2001).

36. Zhu, Y. & Chiarot, P. R. Directed assembly of nanomaterials using electrospray deposition and substrate-level patterning. *Powder Technol.* **364**, 845–850 (2020).

37. Kim, H. *et al.* Parallel patterning of nanoparticles via electrodynamic focusing of charged aerosols. *Nat. Nanotechnol.* **1**, 117–121 (2006).

38. Fang, J. *et al.* Approaching Gas Phase Electrodeposition: Process and Optimization to Enable the Self-Aligned Growth of 3D Nanobridge-Based Interconnects. *Adv. Mater.* **28**, 1770–1779 (2016).

39. Dixkens, J. & Fissan, H. Development of an electrostatic precipitator for off-line particle analysis. *Aerosol Sci. Technol.* **30**, 438–453 (1999).

40. Cao, Z. *et al.* Pool boiling heat transfer of FC-72 on pin-fin silicon surfaces with nanoparticle deposition. *Int. J. Heat Mass Transf.* **126**, (2018).

41. Krinke, T. J., Deppert, K., Magnusson, M. H., Schmidt, F. & Fissan, H. Microscopic aspects of the deposition of nanoparticles from the gas phase. *J. Aerosol Sci.* **33**, 1341–1359 (2002).

42. Kimoto, K., Kamiya, Y., Nonoyama, M. & Uyeda, R. An Electron Microscope Study on Fine Metal Particles Prepared by Evaporation in Argon Gas at Low Pressure. *Jpn. J. Appl. Phys.* **2**, 702–713 (1963).

43. Butter, K., Bomans, P. H. H., Frederik, P. M., Vroege, G. J. & Philipse, A. P. Direct observation of dipolar chains in iron ferrofluids by cryogenic electron microscopy. *Nat. Mater.* **2**, 88–91 (2003).

44. Toulemon, D. *et al.* Enhanced Collective Magnetic Properties Induced by the Controlled Assembly of Iron Oxide Nanoparticles in Chains. *Adv. Funct. Mater.* **26**, 2454–2462 (2016).

45. Balcells, L. *et al.* Spontaneous in-flight assembly of magnetic nanoparticles into macroscopic chains. *Nanoscale* **11**, 14194–14202 (2019).

46. Ekeroth, S. *et al.* Catalytic Nanotruss Structures Realized by Magnetic Self-Assembly in Pulsed Plasma. *Nano Lett.* **18**, 3132–3137 (2018).

47. Lee, G. H., Huh, S. H., Park, J. W., Ri, H. C. & Jeong, J. W. Arrays of ferromagnetic iron and cobalt nanocluster wires. *J. Phys. Chem. B* **106**, 2123–2126 (2002).

48. Athanassiou, E. K., Grossmann, P., Grass, R. N. & Stark, W. J. Template free, large scale synthesis of cobalt nanowires using magnetic fields for alignment. *Nanotechnology* **18**, (2007).

49. Wolf, H. & Birringer, R. Pattern formation in an array of magnetic nanoscale rods mimics magnetic-dipole interaction-driven spinodal decomposition. *J. Appl. Phys.* **98**, (2005).

50. Singh, G. *et al.* Self-assembly of magnetite nanocubes into helical superstructures. *Science (80-.).* **345**, 1149–1153 (2014).

51. Jiang, C., Leung, C. W. & Pong, P. W. T. Magnetic-Field-Assisted Assembly of Anisotropic Superstructures by Iron Oxide Nanoparticles and Their Enhanced Magnetism. *Nanoscale Res. Lett.* (2016).

52. Niu, H., Chen, Q., Zhu, H., Lin, Y. & Zhang, X. Magnetic field-induced growth and self-assembly of cobalt nanocrystallites. *J. Mater. Chem.* **13**, 1803–1805 (2003).

53. Nie, Z., Petukhova, A. & Kumacheva, E. Properties and emerging applications of self-assembled structures made from inorganic nanoparticles. *Nat. Nanotechnol.* **5**, 15–25 (2010).

54. Wang, X. *et al.* Vertically-aligned nanostructures for electrochemical energy storage. *Nano Res.* **12**, 2002–2017 (2019).

55. Yin, J. *et al.* NiO/CoN Porous Nanowires as Efficient Bifunctional Catalysts for Zn-Air Batteries. *ACS Nano* **11**, 2275–2283 (2017).

56. Schwyn, S., Garwin, E. & Schmidt-Ott, A. Aerosol generation by spark discharge. *J. Aerosol Sci.* **19**, 639–642 (1988).

57. Messing, M. E. The advantages of spark discharge generation for manufacturing of nanoparticles with tailored properties. *J. Green Eng.* **5**, 83–96 (2016).

58. Messing, M. E. *et al.* A comparative study of the effect of gold seed particle preparation method on nanowire growth. *Nano Res.* **3**, 506–519 (2010).

59. Feng, J. *et al.* Green manufacturing of metallic nanoparticles: a facile and universal approach to scaling up. *J. Mater. Chem. A* **4**, 11222–11227 (2016).

60. Schmidt-Ott, A. *Spark Ablation: Building Blocks for Nanotechnology*. (Jenny Stanford Publishing Pte. Ltd, 2020).

61. Meuller, B. O. *et al.* Review of spark discharge generators for production of nanoparticle aerosols. *Aerosol Sci. Technol.* **46**, 1256–1270 (2012).

62. Pfeiffer, T. V., Feng, J. & Schmidt-Ott, A. New developments in spark production of nanoparticles. *Adv. Powder Technol.* **25**, 56–70 (2014).

63. Wagner, M., Kohut, A., Geretovszky, Z., Seipenbusch, M. & Galbács, G. Observation of fine-ordered patterns on electrode surfaces subjected to extensive erosion in a spark discharge. *J. Aerosol Sci.* (2016).

64. Kohut, A., Wagner, M., Seipenbusch, M., Geretovszky, Z. & Galbács, G. Surface features and energy considerations related to the erosion processes of Cu and Ni electrodes in a spark discharge nanoparticle generator. *J. Aerosol Sci.* (2018).

65. Tabrizi, N. S., Ullmann, M., Vons, V. A., Lafont, U. & Schmidt-Ott, A. Generation of nanoparticles by spark discharge. *J. Nanoparticle Res.* **11**, 315–332 (2009).

66. Feng, J., Biskos, G. & Schmidt-Ott, A. Toward industrial scale synthesis of ultrapure singlet nanoparticles with controllable sizes in a continuous gas-phase process. *Sci. Rep.* **5**, 1–9 (2015).

67. Koch, W. & Friedlander, S. K. The effect of particle coalescence on the surface area of a coagulating aerosol. *J. Colloid Interface Sci.* **140**, 419–427 (1990).

68. Lehtinen, K. E. J. & Zachariah, M. R. Energy accumulation in nanoparticle collision and coalescence processes. *J. Aerosol Sci.* **33**, 357–368 (2002).

69. Feng, J. *et al.* General Approach to the Evolution of Singlet Nanoparticles from a Rapidly Quenched Point Source. *J. Phys. Chem. C* **120**, 621–630 (2016).

70. Feng, J., Ramlawi, N., Biskos, G. & Schmidt-Ott, A. Internally mixed nanoparticles from oscillatory spark ablation between electrodes of different materials. *Aerosol Sci. Technol.* **52**, 1–10 (2018).

71. Domaschke, M., Schmidt, M. & Peukert, W. A model for the particle mass yield in the aerosol synthesis of ultrafine monometallic nanoparticles by spark ablation. *J. Aerosol Sci.* **126**, 133–142 (2018).

72. Ludvigsson, L., Meuller, B. O. & Messing, M. E. Investigations of initial particle stages during spark discharge. *J. Phys. D. Appl. Phys.* **48**, 314012 (2015).

73. de Zárate, D. O. *et al.* Green and sustainable manufacture of ultrapure engineered nanomaterials. *Nanomaterials* **10**, (2020).

74. Han, K. *et al.* A study of pin-to-plate type spark discharge generator for producing unagglomerated nanoaerosols. *J. Aerosol Sci.* **52**, 80–88 (2012).

75. Chae, S., Lee, D., Kim, M. C., Kim, D. S. & Choi, M. Wire-in-hole-type spark discharge generator for long-time consistent generation of unagglomerated nanoparticles. *Aerosol Sci. Technol.* **49**, 463–471 (2015).

76. Feng, J. *et al.* Unconventional Alloys Confined in Nanoparticles: Building Blocks for New Matter. *Matter* 1–18 (2020).

77. Tabrizi, N. S., Xu, Q., Van Der Pers, N. M., Lafont, U. & Schmidt-Ott, A. Synthesis of mixed metallic nanoparticles by spark discharge. *J. Nanoparticle Res.* **11**, 1209–1218 (2009).

78. Byeon, J. H., Park, J. H. & Hwang, J. Spark generation of monometallic and bimetallic aerosol nanoparticles. *J. Aerosol Sci.* (2008).

79. Muntean, A., Wagner, M., Meyer, J. & Seipenbusch, M. Generation of copper, nickel, and CuNi alloy nanoparticles by spark discharge. *J. Nanoparticle Res.* **18**, (2016).

80. Evans, D. E., Harrison, R. M. & Ayres, J. G. The Generation and Characterization of Metallic and Mixed Element Aerosols for Human Challenge Studies. *Aerosol Sci. Technol.* **37**, 975–987 (2003).

81. Rai, A., Park, K., Zhou, L. & Zachariah, M. R. Understanding the mechanism of aluminium nanoparticle oxidation. *Combust. Theory Model.* **10**, 843–859 (2006).

82. Cabrera, N. & F. Mott., N. Theory of the Oxidation of Metals. *Reports Prog. Phys.* **12**, 163–184 (1949).

83. Linderoth, S., Mørup, S. & Bentzon, M. D. Oxidation of nanometer-sized iron particles. *J. Mater. Sci.* **30**, 3142–3148 (1995).

84. Yao, Y., Hu, Y. & Scott, R. W. J. Watching iron nanoparticles rust: An in situ x-ray absorption spectroscopic study. *J. Phys. Chem. C* **118**, 22317–22324 (2014).

85. Wang, C. M. *et al.* Void formation during early stages of passivation: Initial oxidation of iron nanoparticles at room temperature. *J. Appl. Phys.* **98**, (2005).

86. Shafranovsky, E. A. & Petrov, Y. I. Aerosol Fe nanoparticles with the passivating oxide shell. *J. Nanoparticle Res.* **6**, 71–90 (2004).

87. Fung, K. K., Qin, B. & Zhang, X. X. Passivation of α-Fe nanoparticle by epitaxial γ-Fe2O3shell. *Mater. Sci. Eng. A* **286**, 135–138 (2000).

88. Lee, D. *et al.* Hydrogen-assisted spark discharge generation of highly crystalline and surface-passivated silicon nanoparticles. *J. Aerosol Sci.* **114**, 139–145 (2017).

89. Hallberg, R. T. *et al.* Hydrogen-assisted spark discharge generated metal nanoparticles to prevent oxide formation. *Aerosol Sci. Technol.* **52**, 347–358 (2018).

90. Nanda, K. K., Kruis, F. E. & Fissan, H. Evaporation of Free PbS Nanoparticles: Evidence of the Kelvin Effect. *Phys. Rev. Lett.* **89**, 256103 (2002).

91. Shimada, M., Seto, T. & Okuyama, K. Size change of very fine silver agglomerates by sintering in a heated flow. *Journal of Chemical Engineering of Japan* **27**, 795–802 (1994).

92. Eggersdorfer, M. L. & Pratsinis, S. E. Agglomerates and aggregates of nanoparticles made in the gas phase. *Adv. Powder Technol.* **25**, 71–90 (2014).

93. Nanda, K. K., Maisels, A. & Kruis, F. E. Surface tension and sintering of free gold nanoparticles. *J. Phys. Chem. C* **112**, 13488–13491 (2008).

94. Messing, M. E., Dick, K. A., Wallenberg, L. R. & Deppert, K. Generation of size-selected gold nanoparticles by spark discharge — for growth of epitaxial nanowires. *Gold Bull.* **42**, 20–26 (2009).

95. Nanda, K. K., Maisels, A. & Kruis, F. E. Evolution of crystallinity of free gold agglomerates and shape transformation. *RSC Adv.* **1**, 568–572 (2011).

96. Cho, K., Hogan, C. J. & Biswas, P. Study of the mobility, surface area, and sintering behavior of agglomerates in the transition regime by tandem differential mobility analysis. *J. Nanoparticle Res.* **9**, 1003–1012 (2007).

97. Karlsson, M. N. A. *et al.* Compaction of agglomerates of aerosol nanoparticles: A compilation of experimental data. *J. Nanoparticle Res.* **7**, 43–49 (2005).

98. Williams, M. L. CRC Handbook of Chemistry and Physics, 76th edition. *Occup. Environ. Med.* **53**, 504–504 (1996).

99. Hallberg, R. Aerosol Metal Nanoparticles and their Role in Particle-Assisted Growth of III – V Nanowires. (Lund University, 2018).

100. Magnusson, M. Metal and Semiconductor Nanocrystals for Quantum Devices. (Lund University, 2001).

101. Shin, W. G., Mulholland, G. W. & Pui, D. Y. H. Determination of volume, scaling exponents, and particle alignment of nanoparticle agglomerates using tandem differential mobility analyzers. *J. Aerosol Sci.* **41**, 665–681 (2010).

102. Magnusson, M. H., Deppert, K., Malm, J., Bovin, J. & Samuelson, L. Gold nanoparticles: Production, reshaping, and thermal charging. *J. Nanoparticle Res.* **1**, 243–251 (1999).

103. Blomberg, S. *et al.* Bimetallic nanoparticles as a model system for an industrial NiMo catalyst. *Materials (Basel).* **12**, (2019).

104. White, H. J. Fifty years of electrostatic precipitation. *J. Air Pollut. Control Assoc.* **7**, 166–177 (1957).

105. Pavlish, J. H. *et al.* Status review of mercury control options for coal-fired power plants. *Fuel Process. Technol.* **82**, 89–165 (2003).

106. Scala, F. & Clack, H. L. Mercury emissions from coal combustion: Modeling and comparison of Hg capture in a fabric filter versus an electrostatic precipitator. *J. Hazard. Mater.* **152**, 616–623 (2008).

107. Kettleson, E. M. *et al.* Airborne virus capture and inactivation by an electrostatic particle collector. *Environ. Sci. Technol.* **43**, 5940–5946 (2009).

108. Buggisch, J. R. *et al.* Experimental Model to Test Electrostatic Precipitation Technology in the COVID-19 Era: A Pilot Study. *J. Am. Coll. Surg.* (2020).

109. Baron, P. A., Kulkarni, P. & Willeke, K. *Aerosol Measurement: principles, techniques, and applications*. *Aerosol Measurement* (John Wiley & Sons, INC, 2011).

110. Liu, B. Y. H., Whitby, K. T. & Yu, H. H. S. Electrostatic Aerosol Sampler for Light and Electron Microscopy. *Rev. Sci. Instrum.* **38**, 100–102 (1967).

111. Kala, S., Rouenhoff, M., Theissmann, R. & Kruis, F. E. Synthesis and Film Formation of Monodisperse Nanoparticles and Nanoparticle Pairs. in *Nanoparticles from the Gasphase: Formation, Structure, Properties* (eds. Lorke, A., Winterer, M., Schmechel, R. & Schulz, C.) 99–119 (Springer Berlin Heidelberg, 2012).

112. Fierz, M., Kaegi, R. & Burtscher, H. Theoretical and Experimental Evaluation of a Portable Electrostatic TEM Sampler. *Aerosol Sci. Technol.* **41**, 520–528 (2007).

113. Collins, D. R., Cocker, D. R., Flagan, R. C. & Seinfeld, J. H. The scanning DMA transfer function. *Aerosol Sci. Technol.* **38**, 833–850 (2004).

114. Whitesides, G. M. & Grzybowski, B. Self-assembly at all scales. *Science (80-.).* **295**, 2418–2421 (2002).

115. Grzelczak, M., Vermant, J., Furst, E. M. & Liz-Marzán, L. M. Directed Self-Assembly of Nanoparticles. *ACS Nano* **4**, 3591–3605 (2010).

116. Kralj, S. & Makovec, D. Magnetic Assembly of Superparamagnetic Iron Oxide Nanoparticle Clusters into Nanochains and Nanobundles. *ACS Nano* **9**, 9700–9707 (2015).

117. Townsend, J., Burtovyy, R., Galabura, Y. & Luzinov, I. Flexible chains of ferromagnetic nanoparticles. *ACS Nano* **8**, 6970–6978 (2014).

118. Frey, N. A., Peng, S., Cheng, K. & Sun, S. Magnetic nanoparticles: synthesis, functionalization, and applications in bioimaging and magnetic energy storage. *Chem. Soc. Rev.* **38**, 2532 (2009).

119. Johannsen, M., Thiesen, B., Wust, P. & Jordan, A. Magnetic nanoparticle hyperthermia for prostate cancer. *Int. J. Hyperth.* **26**, 790–795 (2010).

120. Jurgons, R. *et al.* Drug loaded magnetic nanoparticles for cancer therapy. *J. Phys. Condens. Matter* **18**, (2006).

121. Arruebo, M., Fernández-Pacheco, R., Ibarra, M. R. & Santamaría, J. Magnetic nanoparticles for drug delivery. *Nano Today* **2**, 22–32 (2007).

122. Balamurugan, B., Sellmyer, D. J., Hadjipanayis, G. C. & Skomski, R. Prospects for nanoparticle-based permanent magnets. *Scr. Mater.* **67**, 542–547 (2012).

123. Zeng, H., Li, J., Liu, J. P., Wang, Z. L. & Sun, S. Exchange-coupled nanocomposite magnets by nanoparticle self-assembly. *Nature* **420**, 395–398 (2002).

124. Bedanta, S. & Kleemann, W. Supermagnetism. *J. Phys. D. Appl. Phys.* **42**, (2009).

125. Kittel, C. *Introduction to Solid State Physics*. (John Wiley & Sons, INC, 2005).

126. Leslie-Pelecky, D. L. & Rieke, R. D. Magnetic properties of nanostructured materials. *Chem. Mater.* **8**, 1770–1783 (1996).

127. Liu, J. P. Ferromagnetic nanoparticles: Synthesis, processing, and characterization. *Low-dimensional Nanomaterials* **62**, 56–61 (2010).

128. Kneller, E. F. & Luborsky, F. E. Particle Size Dependence of Coercivity and Remanence of Single - Domain Particles. *Journal of Applied Physics* **34**, 656–658 (1963).

129. Sakata, S., Yoshikawa, A. & Tasaki, A. Magnetic separation of aerosol particles from air flow. *Jpn. J. Appl. Phys.* **15**, 2017–2018 (1976).

130. Zarutskaya, T. & Shapiro, M. Capture of nanoparticles by magnetic filters. *J. Aerosol Sci.* **31**, 907–921 (2000).

131. Li, L., Greenberg, P. S., Street, K. W. & Chen, D. R. Study of a magnetic filter system for the characterization of particle magnetic property. *Aerosol Sci. Technol.* **45**, 327–335 (2011).

132. Rogers, H., Anani, T., Choi, Y., Beyers, R. & David, A. Exploiting Size-Dependent Drag and Magnetic Forces for Size-Specific Separation of Magnetic Nanoparticles. *Int. J. Mol. Sci.* **16**, 20001–20019 (2015).

133. Schaller, V. *et al.* Motion of nanometer sized magnetic particles in a magnetic field gradient. *J. Appl. Phys.* **104**, 093918 (2008).

134. Lee, G. H. *et al.* Processing of ferromagnetic iron nanowire arrays. *Scr. Mater.* **49**, 1151–1155 (2003).

135. Krinke, T. J., Fissan, H. & Deppert, K. Deposition of aerosol nanoparticles on flat substrate surfaces. *Phase Transitions* **76**, 333–345 (2003).

136. You, S. & Choi, M. Numerical simulation of microscopic motion and deposition of nanoparticles via electrodynamic focusing. *J. Aerosol Sci.* **38**, 1140–1149 (2007).

137. Rusinque, H., Fedianina, E., Weber, A. & Brenner, G. Numerical study of the controlled electrodeposition of charged nanoparticles in an electric fi eld. *J. Aerosol Sci.* **129**, 28–39 (2019).

138. Kulkarni, P. & Biswas, P. A Brownian dynamics simulation to predict morphology of nanoparticle deposits in the presence of interparticle interactions. *Aerosol Sci. Technol.* **38**, 541–554 (2004).

139. Lindquist, G. J., Pui, D. Y. H. & Hogan, C. J. Porous particulate film deposition in the transition regime. *J. Aerosol Sci.* **74**, 42–51 (2014).

140. Yung, K. W., Landecker, P. B. & Villani, D. D. An Analytic Solution for the Force Between Two Magnetic Dipoles. *Magn. Electr. Sep.* **9**, 39–52 (1998).

141. Correlated Magnetics Research LLC. Differentiate Your Product Design with Polymagnets. *[Report]* (2015).

142. Li, G. & Tang, Z. Noble metal nanoparticle@metal oxide core/yolk-shell nanostructures as catalysts: Recent progress and perspective. *Nanoscale* **6**, 3995–4011 (2014).

143. Chen, M. S. *et al.* Highly active surfaces for CO oxidation on Rh, Pd, and Pt. *Surf. Sci.* **601**, 5326–5331 (2007).

144. Zhou, Y., Wang, Z. & Liu, C. Perspective on CO oxidation over Pd-based catalysts. *Catal. Sci. Technol.* **5**, 69–81 (2015).

145. Eggersdorfer, M. L., Kadau, D., Herrmann, H. J. & Pratsinis, S. E. Multiparticle sintering dynamics: From fractal-like aggregates to compact structures. *Langmuir* **27**, 6358–6367 (2011).

146. Wakai, F. & Brakke, K. A. Tensor virial equation of evolving surfaces in sintering of aggregates of particles by diffusion. *Acta Mater.* **61**, 4103–4112 (2013).

147. Hawa, T. & Zachariah, M. R. Molecular dynamics simulation and continuum modeling of straight-chain aggregate sintering: Development of a phenomenological scaling law. *Phys. Rev. B - Condens. Matter Mater. Phys.* **76**, 1–9 (2007).

148. Molares, M. E. T., Balogh, A. G., Cornelius, T. W., Neumann, R. & Trautmann, C. Fragmentation of nanowires driven by Rayleigh instability. *Appl. Phys. Lett.* **85**, 5337–5339 (2004).

149. Thouy, R., Olivi-Tran, N. & Jullien, R. Fragmentation of two-dimensional mass fractals by surface-diffusion sintering. *Phys. Rev. B* **56**, 5321–5327 (1997).

150. Stokes, D. J. *Principles and Practice of Variable Pressure/Environmental Scanning Electron Microscopy (VP-ESEM)*. *Principles and Practice of Variable Pressure/Environmental Scanning Electron Microscopy (VP-ESEM)* (2008). doi:10.1002/9780470758731

151. Williams, D. B. & Carter, C. B. *Transmission Electron Microscopy: A Textbook for Materials Science*. *Materials Science* (2009). doi:10.1007/978-1-61779-415-5_23

152. Reuter, K. *Operando Research in Heterogeneous Catalysis*. *Springer Series in Chemical Physics* **114**, (Springer International Publishing, 2017).